buildings

MDPI

Article

Flexural Behaviour of Corroded RC Beams Strengthened with CFRCM: Refined Modelling, Parametric Analysis, and Design Assessment

Chaoqun Zeng [1], Jing-Pu Tang [2], Liangliang Wei [3], Miaochang Zhu [4], Ran Feng [5] and Panpan Liu [5,*]

[1] School of Automotive and Transportation Engineering, Shenzhen Polytechnic University, Shenzhen 518055, China; zengchaoqun@szpu.edu.cn
[2] Department of Civil Engineering and Management, University of Manchester, Manchester M13 9PL, UK; jingpu.tang@manchester.ac.uk
[3] School of Environment and Civil Engineering, Dongguan University of Technology, Dongguan 523808, China; liangwei@dgut.edu.cn
[4] School of Civil Engineering and Transportation, Guangzhou University, Guangzhou 510006, China; zhumiaochang@gzhu.edu.cn
[5] School of Intelligent Civil and Ocean Engineering, Harbin Institute of Technology, Shenzhen 518055, China; fengran@hit.edu.cn
* Correspondence: liupanpan@hit.edu.cn

Abstract

Reinforced concrete (RC) beams strengthened with carbon-fabric-reinforced cementitious matrix (CFRCM) systems have shown potential for restoring flexural performance, yet their effectiveness under different corrosion levels remains insufficiently understood. This study presents a numerical investigation of the flexural behaviour of simply supported RC beams externally strengthened with CFRCM plates. Refined finite element models (FEMs) were developed by explicitly incorporating the steel–concrete bond-slip behaviour, the carbon fabric (CF) mesh–cementitious matrix (CM) interface, and the CFRCM–concrete substrate interaction and were validated against experimental results in terms of failure modes, load–deflection responses, and flexural capacities. A parametric study was then conducted to examine the effects of CFRCM layer number, steel corrosion level, and longitudinal reinforcement ratio. The results indicate that the baseline flexural capacity can be fully restored only when the corrosion level remains below approximately 15%; beyond this threshold, none of the CFRCM configurations achieved full recovery. The influence of the reinforcement ratio was found to depend on corrosion severity, while increasing CFRCM layers enhanced flexural performance but exhibited saturation effects for thicker configurations. In addition, corrosion level and CFRCM thickness jointly influenced the failure mode. Comparisons with design predictions show that bilinear CFRCM constitutive models are conservative, whereas existing FRP-based design codes provide closer agreement with numerical and experimental results.

Keywords: carbon fabric reinforced cementitious matrix (CFRCM); corrosion; finite element analysis (FEA); failure modes; interface performance; parametric study

Check for updates

Academic Editor: Duc-Kien Thai

Received: 27 December 2025
Revised: 8 January 2026
Accepted: 12 January 2026
Published: 16 January 2026

Copyright: © 2026 by the authors. Licensee MDPI, Basel, Switzerland. This article is an open access article distributed under the terms and conditions of the Creative Commons Attribution (CC BY) license.

1. Introduction

Reinforced concrete (RC) structures worldwide face persistent durability and performance challenges, particularly those associated with steel corrosion induced by environmental exposure, where they are highly susceptible to long-term chloride-induced

corrosion. In aggressive service environments, RC structures are particularly vulnerable to long-term chloride ingress, which initiates and accelerates corrosion of embedded steel reinforcement, thereby progressively compromising structural integrity and service life [1–4]. As corrosion advances, a gradual reduction in load capacity is commonly observed, which may ultimately result in premature or even catastrophic structural failure [5–8]. Experimental and field evidence indicate that chloride-induced corrosion can cause cumulative cross-sectional losses of up to 40% in tensile steel reinforcement within two decades [9,10], accompanied by a severe deterioration of the steel–concrete bond performance [11,12].

Fibre-reinforced polymer (FRP) systems have been developed to address these issues [13–19]. Malumbela et al. [20] reported that a combined patch-and-FRP technique could mitigate ongoing corrosion while simultaneously enhancing load capacity and stiffness. Masoud and Soudki [21] further observed a 16% reduction in rebar mass loss in FRP-strengthened specimens compared with unstrengthened controls after 152 days of exposure. They also noted that U-shaped glass (G)-FRP wraps effectively suppressed corrosion activity, whereas carbon (C)-FRP plates had a negligible effect. Zidani [22] employed finite element models (FEMs) with material nonlinearity and found that FRP plating improved the flexural capacity of pre-damaged beams, though such improvements were occasionally accompanied by premature debonding failures. Recent studies have extended FRP-based strengthening to continuous RC beams and emphasised the critical role of anchorage and interfacial behaviour in governing strengthening efficiency and failure modes [23,24]. Moreover, advanced numerical modelling and strengthening under degraded material conditions have been reported, providing complementary perspectives on structural performance and model reliability [25,26].

However, their practical use remains limited due to the inherent vulnerability to elevated temperatures and ultraviolet exposure [27,28]. In response, cementitious-based strengthening approaches using engineered cementitious composites (ECC) have been explored for RC structures [29,30]. Fabric-reinforced cementitious matrix (FRCM) systems have emerged as a promising alternative, offering enhanced durability, superior compatibility with concrete substrate, and significantly improved fire resistance [31–33]. Increasing research attention has been directed toward the flexural performance of RC members strengthened with FRCM systems [34–36]. Elghazy et al. [37–39] analysed the critical influence of the cementitious matrix (CM)'s mechanical properties and its interface adhesion to the fabric in governing the failure mechanism and strengthening efficiency. For example, specimens with polyparaphenylene benzobisoxazole (PBO)-FRCM U-wraps typically failed due to matrix fabric slippage, whereas those with carbon-FRCM (CFRCM) exhibited extensive matrix cracking prior to failure [37]. Escrig et al. [40] further highlighted the system-dependent performance of FRCM composites, reporting that steel (S)-FRCM was most effective in restoring flexural capacity, while CFRCM provided the greatest improvement in flexural stiffness. Ebead and El-Sherif [41] added that PBO-FRCM specimens exhibited greater post-yield ductility but also more severe stiffness degradation compared to CFRCM. Moreover, distinct failure modes were observed across fabric types: G-FRCM specimens failed due to fabric rupture, whereas CFRCM and PBO-FRCM systems were prone to delamination.

Beyond experimental investigations, significant efforts have been dedicated to analytically and numerically modelling FRCM systems, with particular emphasis on predicting the effective fabric strain [42–45] and the ultimate load capacity [46–49]. Sneed et al. [42] theorised that the maximum peel strain of S-FRCM was substantially lower than the fabric's fracture strain of 1.5% yet exceeded the 0.34% value from direct shear tests. Subsequently, Bencardino et al. [43] proposed a predictive expression for the peeling strain of S-FRCM, while Zhu et al. [44] developed a strain-based model to determine the effective fabric

strain and establish a criterion for predicting interface failure at either the fibre–mortar or mortar–concrete interface. Jung et al. [45] further demonstrated that sliding-induced debonding between hybrid carbon/glass fabrics and the matrix at high strain levels necessitates bond–slip formulations that explicitly capture this phenomenon. On the theoretical front, Zhou et al. [46] and Wei et al. [47] established analytical formulas for key behavioural stages, including cracking, yielding, and ultimate loads, as well as deflection predictions. Advancing the analysis to member-level behaviour, Mandor and El Refai [48] suggested that FRCM strengthening can facilitate moment redistribution following plastic hinge formation. They proposed a corresponding quantification approach alongside a refined deflection formula that incorporates stiffness degradation [49].

The numerical simulation of FRCM-strengthened members has progressed substantially to complement experimental findings. Elghazy et al. [50] determined that failure is predominantly governed by fibre–matrix slip, a mechanism largely insensitive to the concrete's compressive strength and cover thickness. Consistent with this observation, Aljazaeri et al. [51] demonstrated that the concrete's compressive strength exerts a minimal influence on the ultimate capacity, while the reinforcement ratio remains a decisive parameter. Taie et al. [52] extended the analysis to more complex structural systems by investigating the flexural behaviour of two-span continuous beams strengthened with PBO-FRCM. Their findings highlighted a strong dependency of the flexural response on both the strengthening configuration and the number of layers in both hogging and sagging moment regions. Specifically, the hogging-to-sagging moment ratio was found to significantly influence the failure mode in the hogging region, whereas the beam's overall ductility was primarily governed by the flexural behaviour in the sagging region.

While previous research has provided valuable insights into the flexural performance of FRCM-strengthened systems, notable knowledge gaps remain unaddressed. Existing studies have primarily focused on the influence of different strengthening systems, failure modes, and load capacity enhancement. Although key parameters have been compared and analytical models proposed, a fundamental limitation persists in the field of numerical simulation. Specifically, refined FEMs capable of accurately capturing structural performance under high corrosion rates are still lacking. Moreover, prevailing modelling approaches have tended to overlook the integration of critical interface behaviour, including steel–concrete bond degradation induced by corrosion, the fabric-to-matrix interface, and the FRCM-to-concrete substrate interaction. This omission of interconnected interface data prevents a comprehensive, multi-scale analysis spanning material behaviour, interface response, and full member performance. To bridge these gaps, the present study develops a refined finite element modelling framework that explicitly incorporates the aforementioned interface laws and corrosion effects, thereby enabling a rigorous characterisation of the flexural performance evolution of CFRCM-strengthened RC beams.

This study presents a comprehensive numerical investigation of the flexural behaviour of simply supported RC beams strengthened with CFRCM plates. A refined three-dimensional FEM was developed and rigorously validated against existing experimental data. A pivotal feature of this model is the explicit incorporation of the constitutive laws for all critical interface mechanisms: the bond–slip behaviour between steel and concrete, the stress transfer between carbon fabric (CF) mesh and CM, and the interaction between the CFRCM composite and the concrete substrate. The validated model demonstrated high accuracy in replicating key experimental observations, including crack propagation, load–displacement response, and ultimate bending capacity. Based on this FEM, an extensive parametric study was undertaken to quantify the effects of the number of CFRCM layers, the corrosion level of the steel reinforcement, and the longitudinal reinforcement ratio on the flexural performance. The influences of these parameters on

load recovery, strengthening enhancement, and failure modes were also examined in detail. Finally, the current design codes, including ACI 549.4R-20 [53], ACI 440.2R-17 [17], FIB Bulletin 14 [18], and CECS 146-2003 (2007) [19], were evaluated by comparing their predicted bending capacities with the numerical results.

2. A Brief Summary of Experimental Work

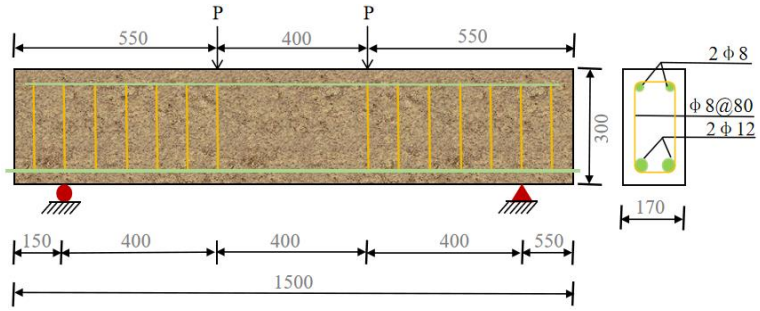
This section provides a concise overview of the experimental programme used to validate the FEM developed in this study. A detailed description of the experimental work can be found in ref. [47]. The test series included one unstrengthened control beam (S-B-L0) and three beams strengthened with one, two, and four CFRCM layers (S-B-L1, S-B-L2, and S-B-L4, respectively). The key material properties of the concrete, tensile steel reinforcement, CM, and dry CF are summarised in Table 1.

Table 1. Material properties.

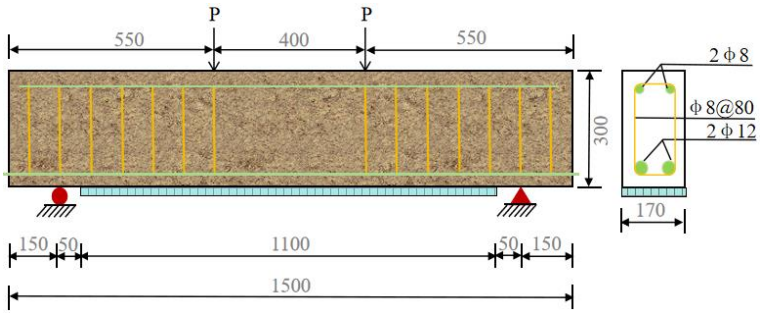
Material	Material Properties	
Concrete	Cubic compressive strength (f_{cu}) (MPa)	42.20
Tensile steel (ϕ 12)	Yielding strength (f_{ly}) (MPa)	496.70
	Yielding strain (ε_{ly}) (%)	0.25
	Tensile strength (f_{lu}) (MPa)	601.30
	Tensile strain (ε_{lu}) (%)	9.30
	Elastic modulus (E_l) (GPa)	200.00
Compressive steel/stirrup (ϕ 8)	Yielding strength (f_{sy}) (MPa)	340.00
	Yielding strain (ε_{sy}) (%)	0.17
	Tensile strength (f_{su}) (MPa)	544.00
	Tensile strain (ε_{su}) (%)	13.00
	Elastic modulus (E_s) (GPa)	200.00
CM	Compressive strength (f_{cmu}) (MPa)	71.50
	Flexural strength (f_{bm}) (MPa)	9.30
Dry CF	Tensile strength (f_{cf}) (MPa)	2125.00
	Elastic modulus (E_{cf}) (GPa)	196.40
	Tensile strain (ε_{cf}) (%)	1.10

The reinforcement layout, specimen dimensions, and boundary conditions are shown in Figure 1. Each specimen had a total length of 1500 mm and a cross-section of 170 × 300 mm. Two 12 mm diameter tensile longitudinal bars were placed at the bottom of the cross-section, and two 8 mm diameter compressive longitudinal bars were positioned at the top, with a concrete cover of 30 mm. Stirrups were omitted within the 400 mm span between the loading points. Beyond this region, stirrups were spaced at 80 mm intervals. The soffit of the beams was sandblasted, followed by the external bonding of a CFRCM plate with a length of 1100 mm to the beam soffit, as shown in Figure 1b. No end anchorage system was adopted herein.

Regarding the failure modes, a classical flexural failure mode was observed in the unstrengthened specimen S-B-L0, characterised by yielding of the longitudinal reinforcement followed by concrete crushing. The strengthened beams S-B-L1 and S-B-L2 exhibited a similar failure mode, governed by slippage of the CF mesh within the mortar matrix of the CFRCM system, followed by concrete crushing. In contract, a sudden and brittle failure was observed in specimen S-B-L4, attributed to the concrete cover peeling off.



(**a**) Details and configurations of unstrengthened control beam



(**b**) Details and configurations of CFRCM-strengthened beam

Figure 1. Details and configurations of specimens (unit: mm).

3. Development of FEMs

In this study, the Displacement Analyzer (DIANA) [54] was employed to simulate the mechanical response of the specimens. Its extensive library of constitutive models makes it well suited to the non-linear analysis of quasi-brittle materials such as concrete. Four three-dimensional FEMs were developed and analysed: one unstrengthened control beam and three CFRCM strengthened beams. The constitutive models adopted for the concrete, CFRCM composite, and steel reinforcement, as well as the theoretical models for the steel–concrete bond interface, the CF mesh–CM interaction interface, and the CFRCM–concrete substrate interface, which are fundamental to establishing the refined FEMs, are detailed. The mesh type, loading, boundary conditions, and solver settings are also reported.

3.1. Simulation of Material Properties

3.1.1. Concrete

The constitutive model for concrete encompasses the total strain crack model, the tensile softening function proposed by Hordijk [55] (Figure 2a), and the parabolic compressive curve introduced by Feenstra [56] (Figure 2b). The full description of this model is provided in ref. [57].

Since only the cubic compressive strength (f_{cu}) of concrete was reported in the test results, the remaining concrete properties used in the model are derived from code-based relationships. The tensile strength is taken as 2.01 MPa in accordance with GB50010-2015 [58], while the cylindrical compressive strength f_c' and elastic modulus E_c are calculated using Equations (1) and (2), respectively [58,59].

$$f_c' = 0.79 f_{cu} \tag{1}$$

$$E_c = 4700\sqrt{f_c'} \tag{2}$$

Within the total strain crack model framework, both tensile and compressive responses are governed by fracture energy. The tensile fracture energy (G_f) is calculated

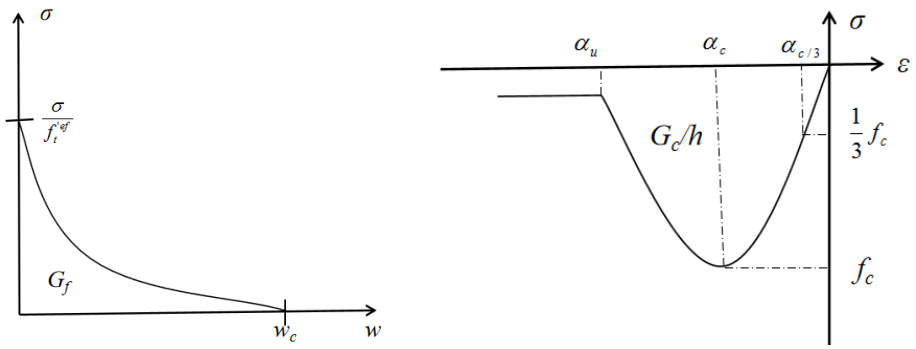
using Equation (3) [60], while the compressive fracture energy (G_c) is determined using Equation (4) [61]. All resultant material parameters used in the finite element analysis (FEA) are summarised in Table 2.

$$G_f = 0.073 f_c'^{0.18} \tag{3}$$

$$G_c = \left(\frac{f_c'}{f_t}\right)^2 G_f \tag{4}$$

Table 2. Material parameters of concrete and CM in the FEA.

Material	Concrete	CM
Cylinder compressive strength (MPa)	33.34	56.49
Tensile strength (MPa)	2.01	4.65
Tensile fracture energy (N/mm)	0.14	0.15
Compressive fracture energy (N/mm)	38.51	27.90
Elastic modulus (MPa)	27.20	27.20
Poisson's ratio	0.20	0.20
Shear retention factor	0.01	0.01



(**a**) (**b**)

Figure 2. Concrete behaviour in tension and compression. (**a**) Crack opening law proposed by Hordijk [48]; (**b**) Parabolic compression curve [49].

3.1.2. CFRCM Composite

The CFRCM composite comprises the CF mesh and CM. In this study, the CF mesh has a fibre spacing of 100 bundles per metre in the primary direction and 130 bundles per metre in the secondary direction. Due to the limitation that the bidirectional reinforcement function in DIANA [54] can only simulate bidirectional CF mesh without capturing bond-slip behaviour, the CF mesh is idealised as a 0.1 mm thick membrane based on the net area of CF [57,62]. Its tensile behaviour is defined by a linear elastic model up to the ultimate tensile strength, whilst its compressive strength is assigned as a nominal value of 0.01 MPa.

The CM, as a quasi-brittle material similar to concrete, is modelled using the fixed total strain crack model. The compressive strength of the CM (f_{mc}) is taken from experimental tests, and the tensile strength (f_{mt}) is calculated according to ACI 318-08 [59], as given by Equation (5). The elastic modulus was assumed to be equivalent to that of concrete.

$$f_{mt} = 0.62\sqrt{f_{mc}} \tag{5}$$

The tensile behaviour of the CFRCM composite is represented by the tensile behaviour of the CF alone in accordance with ACI 549.4R-20 [53]. The tensile constitutive models for one-, two-, and four-layer CF systems are presented in Figure 3. The tensile constitutive

model for the three-layer CF system was derived by linear interpolation between the two- and four-layer models. Specifically, the characteristic points, including the transition point and the peak tensile stress–strain point, were obtained by averaging the corresponding values of the two- and four-layer CF models. The tensile and compressive fracture energies of the CM (G_{fcm} and G_{cm}) are also determined using Equations (3) and (4), and the corresponding values are provided in Table 2.

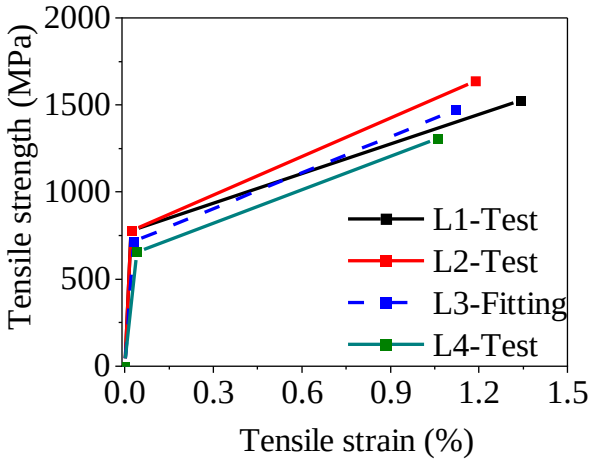


Figure 3. Tensile constitutive models for CF with different numbers of layers.

3.1.3. Reinforcing Steel

In FEA, reinforcing steel is modelled as an isotropic material, with its yield behaviour represented by the von Mises criterion and isotropic strain hardening. The hardening function is directly defined using the stress–strain data obtained from experimental tests, as detailed in ref. [47]. To facilitate the subsequent parametric study and to incorporate the degradation of mechanical properties due to corrosion, the key parameters of the reinforcing steel at various corrosion rates are implemented based on the empirical relationships given in ref. [63], as given by Equations (6)–(10). These parameters include yield strength, ultimate strength, and elastic modulus.

$$f_{y\eta} = (1 - 1.004\eta) f_{y0} \tag{6}$$

$$f_{s\eta} = (1 - 0.834\eta) f_{s0} \tag{7}$$

$$E_{s\eta} = (1 - 0.767\eta) E_{s0} \tag{8}$$

$$\varepsilon_{p\eta} = (1 - 2.231\eta) \varepsilon_{p0} \tag{9}$$

$$\varepsilon_{s\eta} = (1 - 2.159\eta) \varepsilon_{s0} \tag{10}$$

where η represents the corrosion rate, and $f_{y\eta}$, $f_{s\eta}$, $E_{s\eta}$, $\varepsilon_{p\eta}$, and $\varepsilon_{s\eta}$ denote the nominal yield strength, nominal ultimate strength, nominal elastic modulus, initial hardening strain, and peak strain of corroded reinforcing steel, respectively. The parameters f_{y0}, f_{s0}, E_{s0}, ε_{p0}, and ε_{s0} correspond to those properties of the uncorroded reinforcement.

3.2. Interface Behaviour

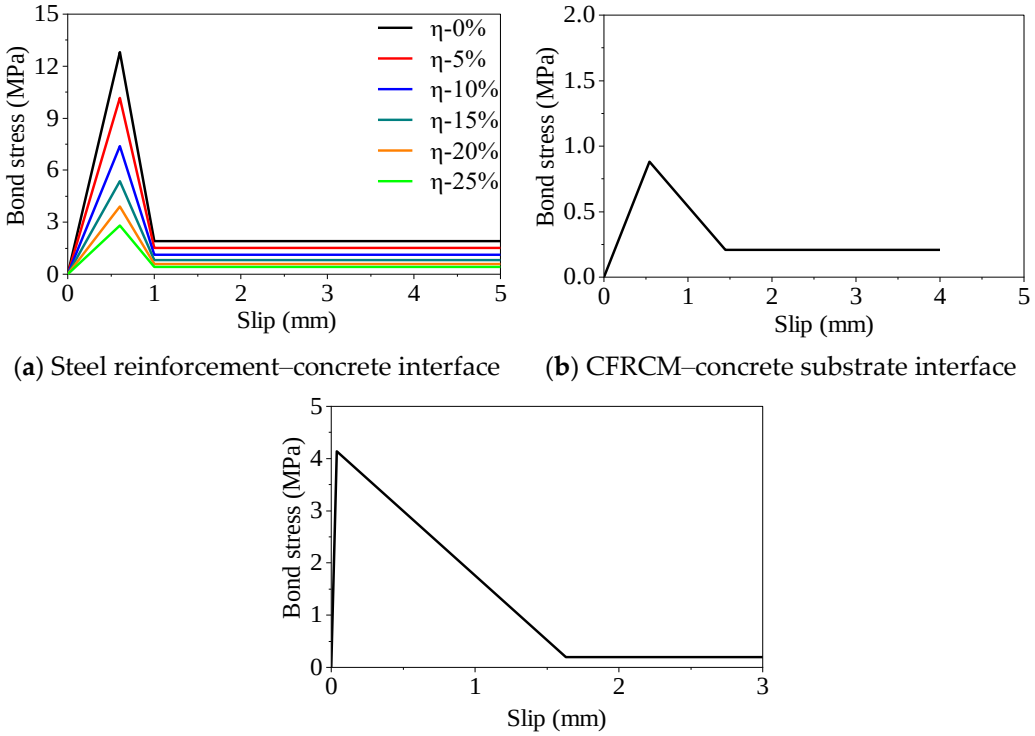
3.2.1. Bond–Slip Model Between Concrete and Steel Reinforcement

The bond performance between steel reinforcement and concrete is highly sensitive to the level of corrosion [11,12], which directly affects the overall effectiveness of CFRCM strengthening. Therefore, accurate simulation of the steel–concrete interface is essential. For

uncorroded reinforcement, the bond–slip constitutive relationship recommended by the CEB-FIP model code [64] is adopted, as given by Equation (11) and illustrated in Figure 4a.

$$\tau = \begin{cases} \tau_{max}\left(\frac{s}{s_1}\right)^{0.4} & 0 \le s \le 0.6 \\ \tau_{max} & 0.6 < s \le 0.6 \\ \tau_{max} - \left(\tau_{max} - \tau_f\right)\left(\frac{s-s_2}{s_3-s_2}\right) & 0.6 < s \le 1.0 \\ \tau_f & s > 1.0 \end{cases} \quad (11)$$

where τ is the local bonding strength, τ_{max} is the maximum local bonding strength, and s is the local slip.



(**a**) Steel reinforcement–concrete interface (**b**) CFRCM–concrete substrate interface

(**c**) CM-CF interface

Figure 4. Bond–slip models for steel–concrete, CFRCM–concrete, and CM-CF interfaces.

It should be noted that corrosion in real RC structures often develops in a non-uniform manner, whereas the corrosion level considered in this study is idealised as an equivalent uniform mass loss calibrated from laboratory observations. This assumption enables a consistent representation of corrosion effects in member-level parametric analyses.

To adequately account for the bond performance of corroded reinforcement in subsequent parametric study, a reduction factor (R_c) is applied to the bond strength. The resulting bond characteristic strength ($\tau_{max}(\eta)$) for corroded reinforcement is determined following the methodology proposed in ref. [11], as given by Equations (12)–(14):

$$\tau_{max}(\eta) = \tau_{max} R_c = \tau_{max} R_{st}\ R_m \quad (12)$$

$$R_{st} = 1 - 0.68\ \eta_{stave} \quad (13)$$

$$R_m = \begin{cases} 1 & \eta \le 1.5\% \\ e^{-\delta(\eta - 1.5\%)} & \eta > 1.5\% \end{cases} \quad (14)$$

where R_{st} and R_m are the coefficients that represent the influence of stirrup corrosion and longitudinal bar corrosion on bond strength, respectively, while η_{stave} is the average percentage of mass loss in steel reinforcement. δ is determined by Equations (15) and (16) [11].

$$\delta = \frac{k_1 + k_2(c/d_b)}{k_4\xi_{st} + 1} \tag{15}$$

$$\xi_{st} = n_{st}A_{st}/(n_b d_b s_{st}) \tag{16}$$

where k_1, k_2, and k_4 are 13.28, −0.57, and 43.54, respectively; c is the concrete cover; d_b is the initial diameter of the longitudinal bar; n_{st} is the number of stirrups that cross the splitting plane; n_b is the number of longitudinal bars; and s_{st} is the stirrup spacing.

3.2.2. CFRCM Composite–Concrete Substrate Interface

The interface between the CFRCM composite and the concrete substrate is characterised by the bond between the CM and the concrete. This interface was modelled using a trilinear cohesive zone law, as defined in Equation (17). The specific parameters for this model are determined based on the experimental data and analytical procedure reported by Liu et al. [65], as given by Equations (18)–(23). The constitutive relationship for this interface is illustrated in Figure 4b.

$$\tau = \begin{cases} k_1 s & 0 \le s < s_{max} \\ \tau_{max} - k_2\left(s - \frac{\tau_{max}}{k_1}\right) & s_{max} \le s < s_0 \\ \tau_0 & s_0 \le s \end{cases} \tag{17}$$

where k_1 and k_2 are the rising slope and the descending slope of the trilinear bond–slip curve, respectively; τ_{max} and τ_0 are the ultimate shear strength and residual bond stress of the FRCM–concrete interface, respectively; s_{max} is the interface slip corresponding to the ultimate shear strength; and s_0 is the slip at the residual bond stress.

$$K_1 = E_f A_f \lambda_1 tanh(\lambda_1 L) \tag{18}$$

$$\lambda_1 = \sqrt{\frac{ck_1}{E_f A_f}} \tag{19}$$

$$K_2 = E_f A_f tan(\lambda_2 L) \tag{20}$$

$$\lambda_1 = \sqrt{\frac{ck_2}{E_f A_f}} \tag{21}$$

$$\tau_{max} = \frac{P_{max}\lambda_2}{csin(\lambda_2 L)} \tag{22}$$

$$\tau_0 = \frac{P_0}{cL} \tag{23}$$

where K_1 and K_2 represent the initial slope and deteriorated slope of experimental curve, respectively; E_f and A_f is elastic modulus and cross-sectional area of CF, respectively; c is the perimeter of the cross-section of CF; L is the bonding length; and P_0 is the load corresponding to the friction stage.

3.2.3. Cementitious Matrix-CF Interface

The bond–slip relationship for the interface between the CM and CF is taken from a previous study [62]. The interface properties are assumed to represent short- to medium-term conditions, and the long-term degradation effects induced by environmental actions

(e.g., moisture exposure, freeze–thaw cycles, or cyclic loading) are not explicitly considered. Since no delamination failure was observed in the CFRCM-strengthened specimens, the bond–slip relationship corresponding to the higher bond strength is selected for this investigation. The resulting constitutive relationship for this interface is presented in Figure 4c.

3.3. Sensitivity Analysis and Mesh Type

A mesh sensitivity analysis is performed to determine the optimal mesh size. Three mesh sizes (20 mm, 30 mm, and 40 mm) are evaluated for specimen S-B-L1 to establish an appropriate balance between computational cost and numerical accuracy. The corresponding FEA runtimes were 6 h, 4 h, and 1.5 h, with deviations of 1.28%, 1.23%, and 1.43%, respectively, from the experimental results. Based on these results, a mesh size of 30 mm is selected for all subsequent simulations as it provides a good compromise between computational efficiency and accuracy.

Figure 5 gives the FEM of strengthened specimen. It can be seen that the CHX60 element, a twenty-node isoparametric solid brick element employing quadratic interpolation and Gauss integration, is used to model the concrete, CM, and cushion block due to its computational efficiency. The CQ40S element, an eight-node quadrilateral isoparametric curved shell element, is selected for the CF mesh. All interfaces are modelled using the CQ48I element, a specialised interface element designed to connect two surfaces in a three-dimensional configuration.

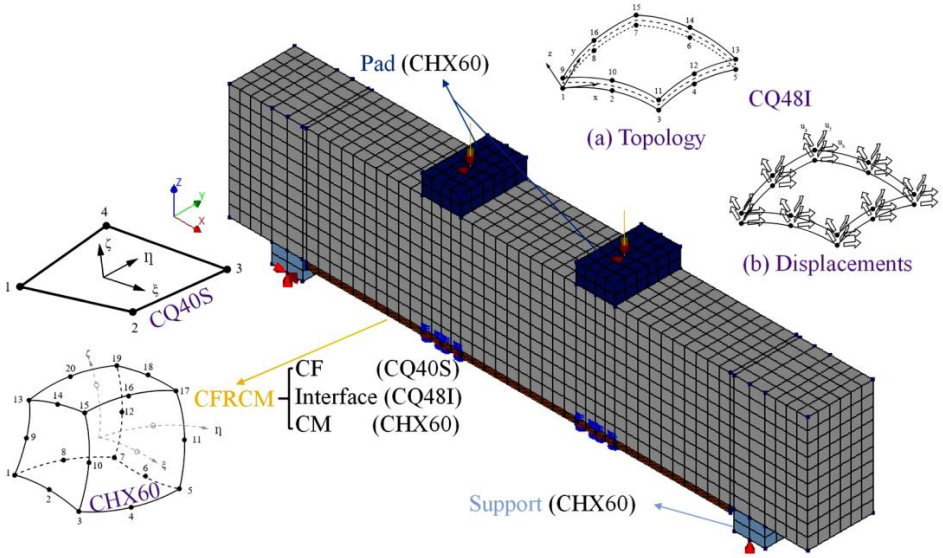


Figure 5. FEM of strengthened specimen.

3.4. Loading and Boundary Conditions

Accurate boundary conditions are essential to replicate experimental conditions. Out-of-plane displacements and rotations are restrained at both supports to simulate realistic boundary behaviour. Horizontal and vertical displacements are fixed at the left support, while only vertical displacement is fixed at the right support to satisfy the simply supported boundary requirements. To streamline the FEA, the distributed loads applied in the experiment are converted into concentrated loads coupled at the cushion block. At the loading point, displacements in the horizontal and out-of-plane directions are restrained. A displacement-controlled loading scheme is applied at a rate of 0.1 mm per analysis increment, and the Newton–Raphson iteration is employed with dual convergence criteria based on force and displacement.

4. Validation of FEMs

Upon developing the FEMs, the FEA results, including crack pattern, load–displacement response, ultimate loads, and bending moments, are obtained and compared with the experimental results reported in [47], as presented in the following subsections.

4.1. Failure Modes

Figure 6 presents a comparison between the simulated and experimentally observed crack patterns. For the control beam, the simulated cracks are primarily concentrated around the two loading points, with the crack distribution closely matching the experimental results. In specimen S-B-L1, two distinct cracks are observed on the concrete and CM surfaces within the loading region, which aligns with the experimental findings. The crack distribution is more uniform in specimens S-B-L2 and S-B-L4 compared with S-B-L1. In specimen S-B-L2, three cracks develop on the concrete surface, showing good agreement with the experimental crack pattern. For specimen S-B-L4, the experimental image does not clearly reveal the detailed crack distribution, making a direct comparison more difficult. Nevertheless, the specimen shows no significant delamination of the externally bonded layer, and the concrete surface displays denser and finer cracking relative to the other strengthened specimens. The CM surface of S-B-L4 shows the greatest number of cracks, albeit with the smallest crack widths. Overall, the failure modes of the specimens are captured accurately by the FEA, as evidenced by the comparison of simulated and observed fracture patterns.

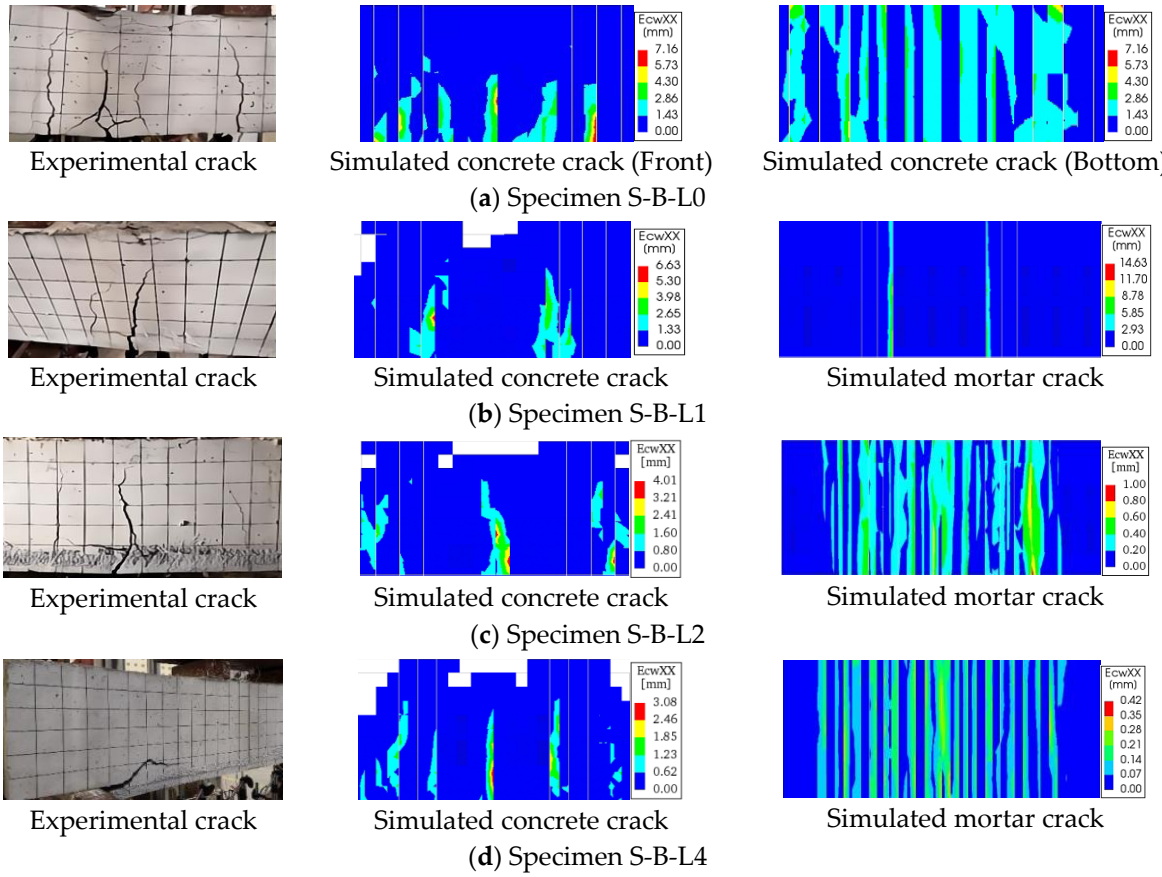
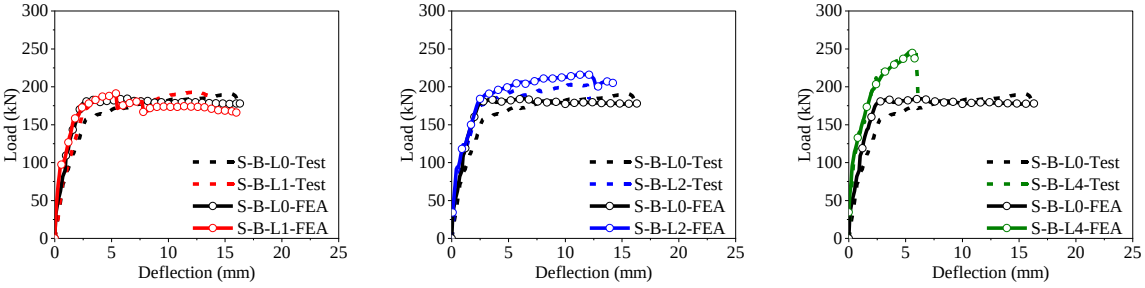


Figure 6. Comparison of crack patterns of specimens.

4.2. Load-Deflection Curves

Figure 7 compares the simulated load–displacement curves and corresponding experimental results. The initial elastic stiffness of the simulated curves is higher than that

of the experimental curves. This discrepancy can be attributed to the fact that the FEMs incorporate only the initial elastic modulus of the materials, whereas in the actual tests, the progressive cracking of concrete and CM leads to a gradual reduction in stiffness. Therefore, some deviations between the experimental and numerical curves are observed.



(**a**) Specimen S-B-L1 (**b**) Specimen S-B-L2 (**c**) Specimen S-B-L4

Figure 7. Comparison of load–deflection curves.

For the control beam (S-B-L0), the stiffness of the experimental and simulated curves agrees well prior to cracking. As the load increases, the FEM predicts that a single dominant crack initiates at mid-span and subsequently propagates symmetrically. In contrast, the experimental crack pattern initiates and develops asymmetrically, which may be attributed to unavoidable minor imperfections in the test setup. This difference results in a deviation between the two curves, particularly after yielding of the steel reinforcement. The simulated load–displacement curve reaches a plateau due to the idealised symmetric crack propagation and deformation development in the FEM, whereas the test curve continues to exhibit a slight increase in load capacity, sustained by the asymmetric crack distribution observed in the test. Overall, a close agreement is observed between the failure loads predicted by the FEA and those obtained from the experimental tests.

The cracking load ($P_{cr,FEA}$), yield load ($P_{y,FEA}$), and ultimate load ($P_{u,FEA}$) obtained from the FEA are compared with the corresponding experimental results (P_{cr}, P_y, and P_u) in Table 3. The mean ratio values of $P_{cr}/P_{cr,FEA}$, $P_y/P_{y,FEA}$, and $P_u/P_{u,FEA}$ are 1.02, 1.00, and 1.01, with coefficient of variation (COV) values of 8.8%, 7.5%, and 4.2%, respectively, demonstrating the high accuracy of the FEA predictions.

Table 3. Comparison of key load values.

Specimens	Experimental Values (kN)			Simulated Values (kN)			Ratios		
	P_{cr}	P_y	P_u	$P_{cr,FEA}$	$P_{y,FEA}$	$P_{u,FEA}$	$P_{cr}/P_{cr,FEA}$	$P_y/P_{y,FEA}$	$P_u/P_{u,FEA}$
S-B-L0	68.30	156.30	191.15	70.67	170.04	184.20	0.97	0.92	1.04
S-B-L1	77.21	170.20	193.72	70.36	170.10	191.20	1.10	1.00	1.01
S-B-L2	84.07	172.10	204.02	91.31	174.81	216.30	0.92	0.98	0.94
S-B-L4	102.81	212.80	251.60	93.94	193.14	245.08	1.09	1.10	1.03
Mean (COV)	—	—	—	—	—	—	1.02 (8.8%)	1.00 (7.5%)	1.01 (4.2%)

For specimen S-B-L1, two important cracks appeared on the surface of the concrete and CFRCM plates, corresponding to the two drops in load observed in the simulated curve. The close agreement between the simulated cracking loads of S-B-L1 and S-B-L0 indicates that a single CFRCM layer provides negligible improvement to the initial cracking resistance. After the failure of CFRCM plate, the load of S-B-L1 is even slightly lower than that of control beam S-B-L0. For specimen S-B-L2, the ductility is improved by CFRCM

strengthening. Prior to failure, the load dropped rapidly to the yield level due to the sudden propagation of the main crack. Meanwhile, the stiffness of specimen S-B-L4 was the highest among all strengthened specimens, resulting in a decrease in ductility to some extent. Failure occurred at a loading displacement of approximately 6 mm, where the simulated curve showed good agreement with the test data.

Overall, the load–displacement curves accurately capture the mechanical response of specimens throughout the loading process. Although inevitable experimental variations lead to certain discrepancies, the FEM developed herein proves essential for reliably reproducing the mechanical behaviour of the specimens.

4.3. Bending Moment

Figure 8 presents a comparison between the simulated cracking moment ($M_{cr,FEA}$), yield moment ($M_{y,FEA}$), and ultimate moment ($M_{u,FEA}$) with the corresponding experimental values (M_{cr}, M_y, M_u). The $M_{cr}/M_{cr,FEA}$, $M_y/M_{y,FEA}$, and $M_u/M_{u,FEA}$ ratios all fall within the range of 0.80–1.20 [66], demonstrating good agreement between the simulation and experimental results.

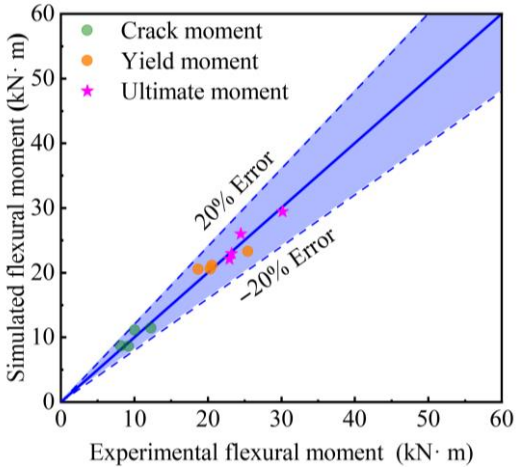


Figure 8. Comparison of key bending moment values.

5. Parametric Study

5.1. General

Upon validation, a parametric study was conducted to systematically investigate the influence of the number of CFRCM layers, the reinforcement ratio, and the corrosion rate of steel reinforcement on the flexural behaviour of the specimens. These parameters were selected due to their significant impact on the load capacity and overall mechanical performance. Specifically, steel corrosion is known to degrade structural integrity by reducing the effective cross-sectional area of the reinforcement and weakening the bond with the surrounding concrete [10,11].

A total of 56 models were developed herein, all maintaining consistency with the validated reference model in terms of mesh size, boundary conditions, and reinforcement layout. The interfacial interactions between steel and concrete, CF and CM, and the CFRCM and concrete substrate were explicitly modelled to accurately capture the composite behaviour. The ultimate loads ($P_{u,FEA}$) and moments ($M_{u,FEA}$) obtained from all models are summarised in Table 4. Notations L0 to L4 in the specimen labelling system indicate the number of applied CFRCM layers, ranging from 0 to 4, while suffixes η_0 to η_5 represent corrosion levels ranging from 0% to 25%, facilitating a structured analysis of the effects of both strengthening and corrosion on structural performance.

Table 4. Model detail and load capacity comparison.

Specimen	Reinforcement Ratio (%)	Corrosion Rate (%)	$P_{u,FEA}$ (kN)	$M_{u,FEA}$ (kN·m)	Specimen	Reinforcement Ratio (%)	Corrosion Rate (%)	$P_{u,FEA}$ (kN)	$M_{u,FEA}$ (kN·m)
S-B-L0	0.52	0.00	184.20	36.81	S-B-L0-d14-η_0	0.71	0.00	199.29	39.86
S-B-L0-d12-η_1	0.52	5.00	179.21	35.84	S-B-L0-d14-η_1	0.71	5.00	193.24	38.65
S-B-L0-d12-η_2	0.52	10.00	168.21	33.64	S-B-L0-d14-η_2	0.71	10.00	185.27	37.05
S-B-L0-d12-η_3	0.52	15.00	159.72	31.94	S-B-L0-d14-η_3	0.71	15.00	175.46	35.09
S-B-L0-d12-η_4	0.52	20.00	151.23	30.25	S-B-L0-d14-η_4	0.71	20.00	152.03	30.41
S-B-L0-d12-η_5	0.52	25.00	133.25	26.65	S-B-L0-d14-η_5	0.71	25.00	123.73	24.75
S-B-L1	0.52	0.00	191.20	38.24	S-B-L1-d14-η_0	0.71	0.00	217.37	43.47
S-B-L1-d12-η_1	0.52	5.00	186.75	37.35	S-B-L1-d14-η_1	0.71	5.00	211.02	42.20
S-B-L1-d12-η_2	0.52	10.00	182.55	36.51	S-B-L1-d14-η_2	0.71	10.00	200.33	40.07
S-B-L1-d12-η_3	0.52	15.00	176.54	35.31	S-B-L1-d14-η_3	0.71	15.00	192.65	38.53
S-B-L1-d12-η_4	0.52	20.00	169.44	33.89	S-B-L1-d14-η_4	0.71	20.00	180.27	36.05
S-B-L1-d12-η_5	0.52	25.00	159.26	31.85	S-B-L1-d14-η_5	0.71	25.00	169.78	33.96
S-B-L2	0.52	0.00	216.30	43.26	S-B-L2-d14-η_0	0.71	0.00	231.84	46.37
S-B-L2-d12-η_1	0.52	5.00	210.85	42.17	S-B-L2-d14-η_1	0.71	5.00	229.54	45.91
S-B-L2-d12-η_2	0.52	10.00	204.61	40.92	S-B-L2-d14-η_2	0.71	10.00	217.29	43.46
S-B-L2-d12-η_3	0.52	15.00	181.74	36.35	S-B-L2-d14-η_3	0.71	15.00	188.96	37.79
S-B-L2-d12-η_4	0.52	20.00	173.32	34.66	S-B-L2-d14-η_4	0.71	20.00	182.42	36.48
S-B-L2-d12-η_5	0.52	25.00	153.23	30.65	S-B-L2-d14-η_5	0.71	25.00	168.10	33.62
S-B-L3-d12-η_0	0.52	0.00	229.50	45.90	S-B-L3-d14-η_0	0.71	0.00	250.40	50.08
S-B-L3-d12-η_1	0.52	5.00	226.84	45.37	S-B-L3-d14-η_1	0.71	5.00	247.09	49.42
S-B-L3-d12-η_2	0.52	10.00	207.70	41.54	S-B-L3-d14-η_2	0.71	10.00	228.90	45.78
S-B-L3-d12-η_3	0.52	15.00	183.71	36.74	S-B-L3-d14-η_3	0.71	15.00	194.12	38.82
S-B-L3-d12-η_4	0.52	20.00	178.06	35.61	S-B-L3-d14-η_4	0.71	20.00	189.89	37.98
S-B-L3-d12-η_5	0.52	25.00	166.79	33.36	S-B-L3-d14-η_5	0.71	25.00	182.45	36.49
S-B-L4	0.52	0.00	245.08	49.02	S-B-L4-d14-η_0	0.71	0.00	269.28	53.86
S-B-L4-d12-η_1	0.52	5.00	226.31	45.26	S-B-L4-d14-η_1	0.71	5.00	250.30	50.06
S-B-L4-d12-η_2	0.52	10.00	208.37	41.67	S-B-L4-d14-η_2	0.71	10.00	224.51	44.90
S-B-L4-d12-η_3	0.52	15.00	190.81	38.16	S-B-L4-d14-η_3	0.71	15.00	187.81	37.56
S-B-L4-d12-η_4	0.52	20.00	184.93	36.99	S-B-L4-d14-η_4	0.71	20.00	184.15	36.83
S-B-L4-d12-η_5	0.52	25.00	167.77	33.55	S-B-L4-d14-η_5	0.71	25.00	187.85	37.57

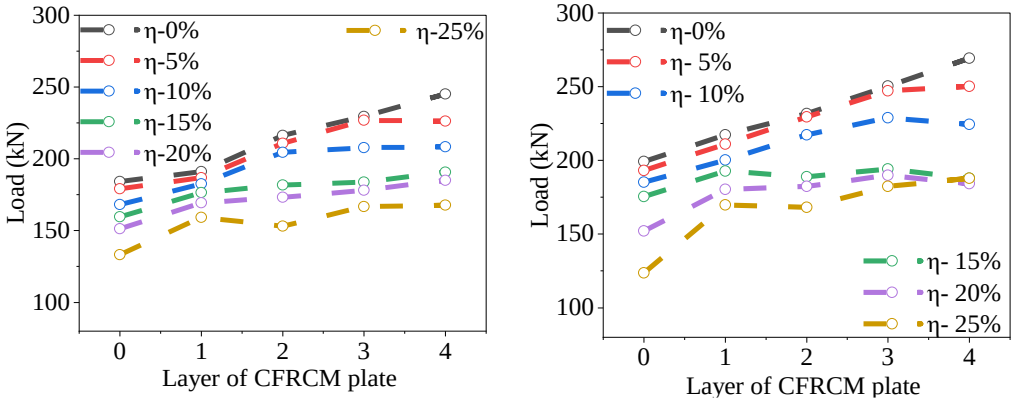
5.2. Load Capacity Comparison

5.2.1. Influence of CFRCM Layer

Figure 9 illustrates the variation in ultimate load capacity with the number of CFRCM layers under two reinforcement ratios. For specimens with a reinforcement ratio of 0.52%, the load capacity increases steadily from L0 to L3 across all corrosion levels. However, once the corrosion level exceeds 5%, the difference between the L3 and L4 configurations becomes negligible, indicating the onset of a saturation effect.

For specimens with a reinforcement ratio of 0.71%, this saturation behaviour becomes more pronounced. When the corrosion level exceeds 10%, the four-layer configuration not only fails to provide additional enhancement but even results in slightly lower capacities than the three-layer configuration. This trend suggests an over-strengthening effect, where the added CFRCM layers cannot be fully utilised due to limitations in interface bond or insufficient deformation compatibility with the internal reinforcement.

Across both reinforcement ratios, the most significant improvement occurs from L1 to L2, while the gains from L2 to L3 are moderate and those from L3 to L4 are minimal. This behaviour highlights a diminishing return in strengthening efficiency as the number of CFRCM layers increases, particularly under higher corrosion levels.



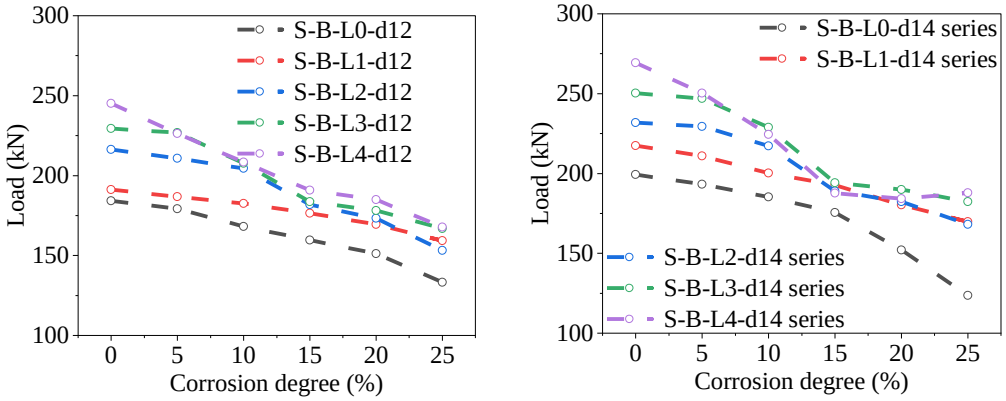
(**a**) Load comparison with different numbers of layers and reinforcement ratio of 0.52%

(**b**) Load comparison with different numbers of layers and reinforcement ratio of 0.71%

Figure 9. Effect of CFRCM layer number on load capacity.

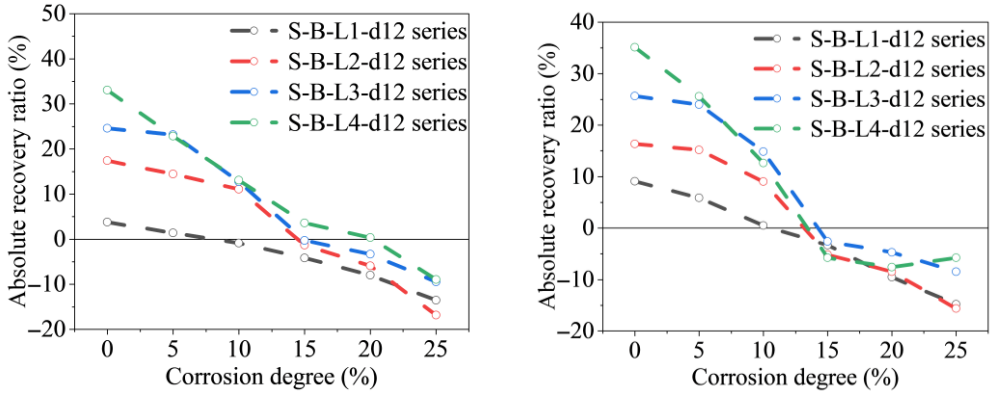
5.2.2. Influence of Corrosion Rate of Steel Reinforcement

Figure 10a,b show that the load capacity of specimens gradually decreases with an increasing corrosion rate, reflecting the combined effects of steel cross-sectional loss and bond degradation between the steel and surrounding concrete [10,11]. To evaluate the rehabilitation capability of the CFRCM system, Figure 10c,d present the absolute recovery ratio, defined relative to the uncorroded, unstrengthened specimens.



(**a**) Load comparison of specimens with a reinforcement ratio of 0.52%

(**b**) Load comparison of specimens with a reinforcement ratio of 0.71%



(**c**) Absolute recovery ratio with a reinforcement ratio of 0.52%

(**d**) Absolute recovery ratio with a reinforcement ratio of 0.71%

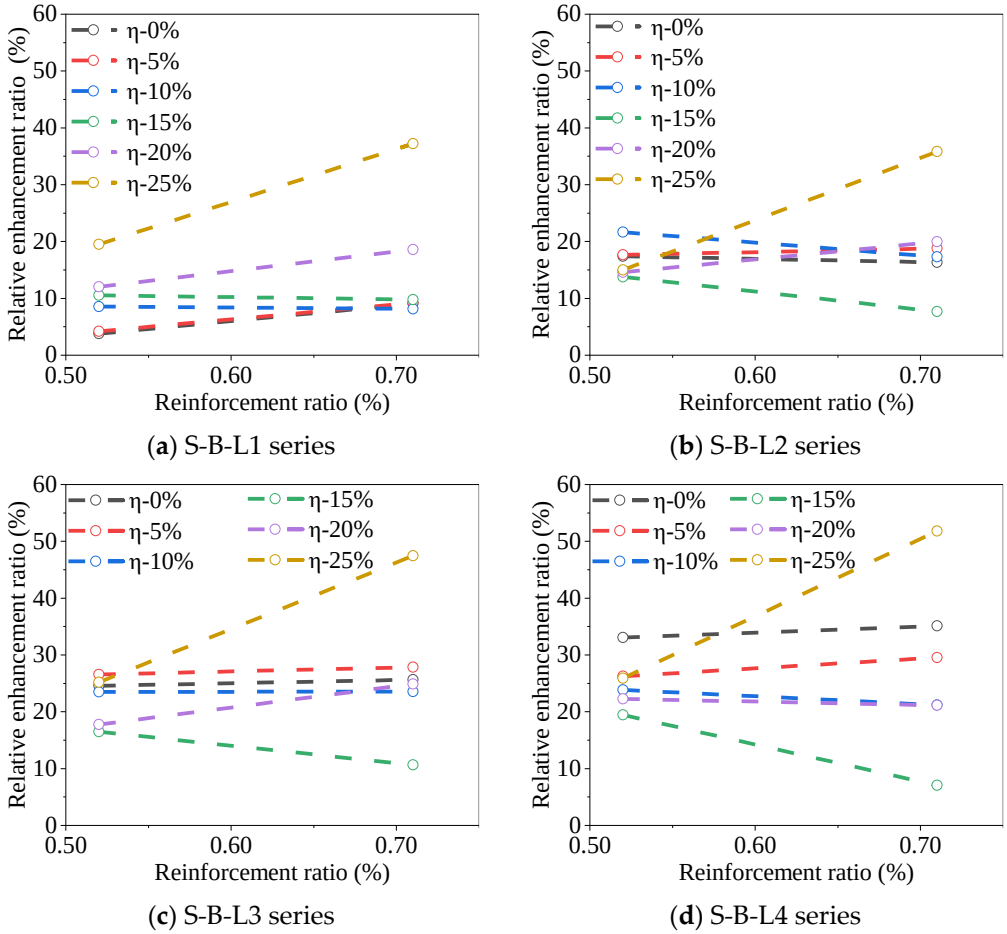
Figure 10. Effect of corrosion rate on load capacity.

For specimens with a reinforcement ratio of 0.52%, a single CFRCM layer is sufficient to restore the load capacity to the uncorroded unstrengthened baseline level when the corrosion rate remains below 10%. When corrosion reaches 15%, L2 or L3 is required to recover the baseline capacity, whereas at 20% corrosion, only L4 can achieve full recovery.

For specimens with a reinforcement ratio of 0.71%, the ultimate load can be restored to the baseline level within a corrosion rate of approximately 10% by using a single layer. However, once the corrosion rate reaches around 13%, the recovery levels achieved by L2, L3, and L4 become relatively close, indicating only limited additional benefit from increasing the number of layers. At a corrosion level of 25%, all strengthening configurations exhibit a 10–20% reduction in capacity compared to the uncorroded, unstrengthened baseline, indicating a significantly reduced effectiveness of the strengthening system. Overall, the baseline capacity can be recovered when corrosion remains below 10–15%; however, beyond this threshold, full recovery is no longer achievable regardless of the number of CFRCM layers.

5.2.3. Influence of Reinforcement Ratio

Figure 11 presents the relative enhancement ratio, defined as the percentage increase in ultimate load of the strengthened specimens compared with the unstrengthened ones at the same corrosion level. The results indicate that the influence of reinforcement ratio highly depends on corrosion severity.



(**a**) S-B-L1 series (**b**) S-B-L2 series

(**c**) S-B-L3 series (**d**) S-B-L4 series

Figure 11. Effect of reinforcement ratio on load capacity.

When the corrosion level is not greater than 10%, the enhancement ratios for the two reinforcement ratios (0.52% and 0.71%) are almost identical, and the curves remain nearly horizontal, indicating that the reinforcement ratio has only a minor effect at this

stage. Once the corrosion level exceeds 10%, the effect becomes more pronounced. At 15% corrosion, all configurations with a reinforcement ratio of 0.52% exhibit higher enhancement ratios than those with 0.71%, with the difference being most evident for the four-layer configuration. When the corrosion level reaches 20%, this difference diminishes and, in some cases, begins to reverse. At 25% corrosion, a clear and consistent pattern emerges across all configurations: specimens with a reinforcement ratio of 0.71% show markedly higher enhancement ratios than those with 0.52%, as reflected by the upward shift in the yellow dashed lines.

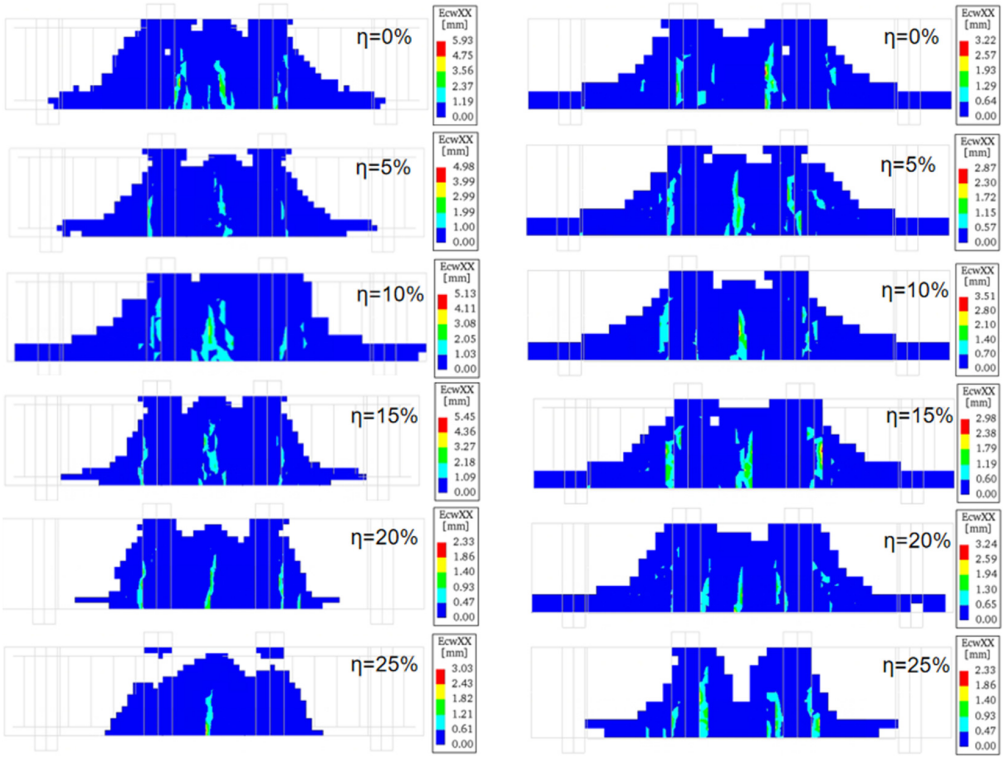
Overall, up to a corrosion level of about 15%, specimens with a reinforcement ratio of 0.52% tend to achieve higher or comparable enhancement ratios, whereas beyond 15% corrosion, those with 0.71% reinforcement consistently provide superior strengthening effectiveness.

5.3. Failure Modes Summary

Figures 12 and 13 present the crack patterns on the concrete surface and CFRCM layers for specimens with a reinforcement ratio of 0.52%. The failure characteristics varied systematically with the number of CFRCM layers and the corrosion level.

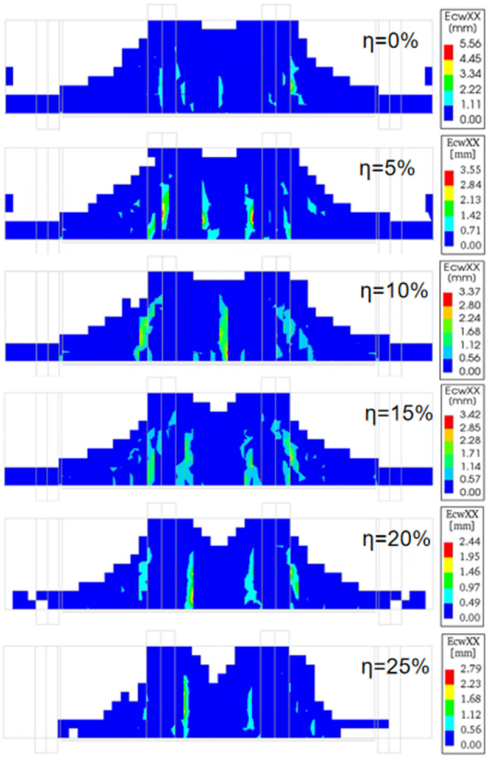
For the unstrengthened specimens, multiple flexural cracks were observed at low corrosion levels. As corrosion increased, these cracks progressively concentrated into a single dominant crack at 25% corrosion (Figure 12a), reflecting a transition from ductile to brittle response.

For the L1-L2 series, well-distributed flexural cracks were maintained when corrosion was below 15%, and fine, uniform cracking was also observed on the CFRCM surface (Figure 13a,b), indicating effective stress redistribution. When corrosion increased to the 20–25% range, the overall crack pattern became notably less uniform, and larger uncracked regions developed on both the concrete and CFRCM surfaces. These changes reflect progressive deterioration of the steel–concrete bond and a reduced deformation capacity of the section under higher corrosion levels.

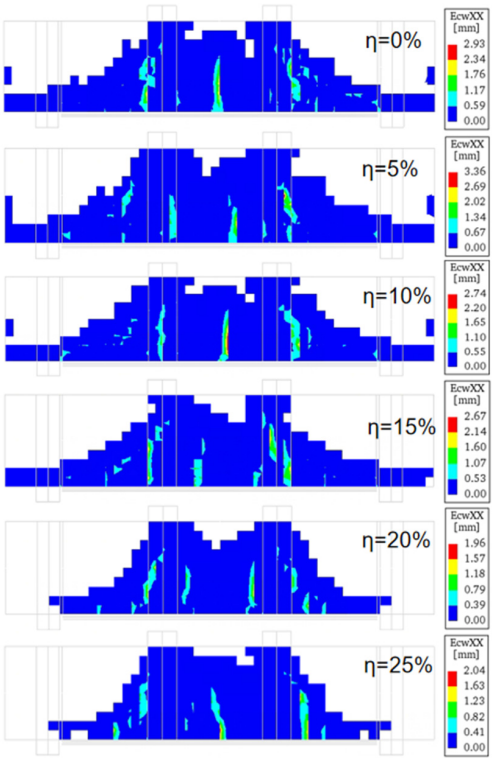


(**a**) S-B-L0-d14 series (**b**) S-B-L1-d14 series

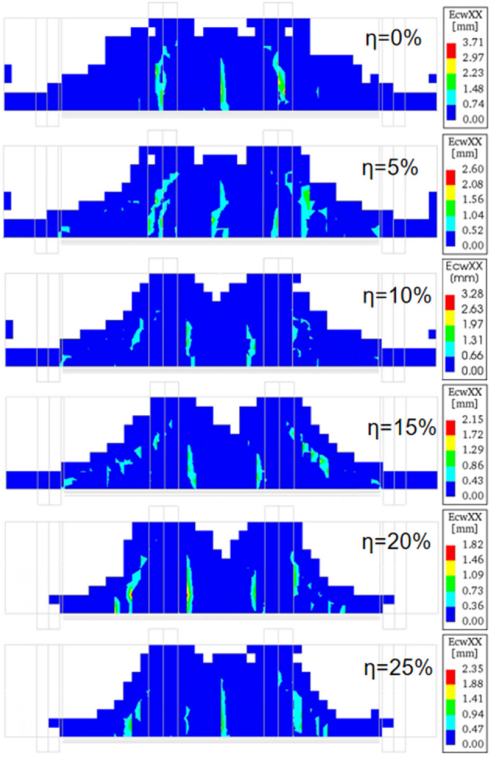
Figure 12. *Cont.*



(**c**) S-B-L2-d14 series



(**d**) S-B-L3-d14 series



(**e**) S-B-L4-d14 series

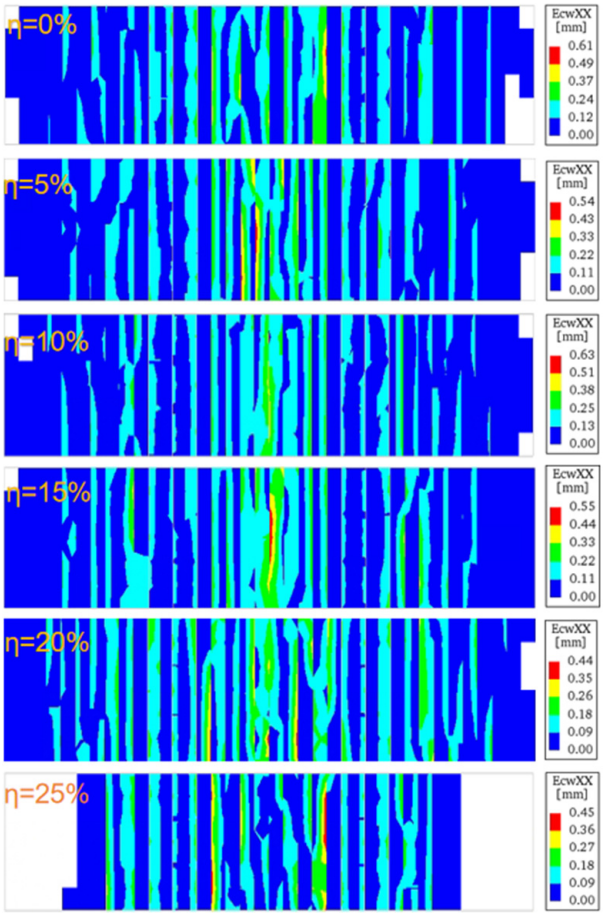
Figure 12. Concrete crack patterns under different corrosion rates and CFRCM layer numbers.

The L3–L4 series exhibited a noticeably different failure pattern compared with the L1–L2 specimens. At low corrosion levels ($\eta \leq 10\%$), the CFRCM plates develop dense and continuous crack bands along most of the span, while the concrete surface is dominated by flexural cracks (Figures 12d,e and 13c,d). This indicates that the external reinforcement is effectively engaged and that the internal reinforcement still provides a relatively uniform flexural response.

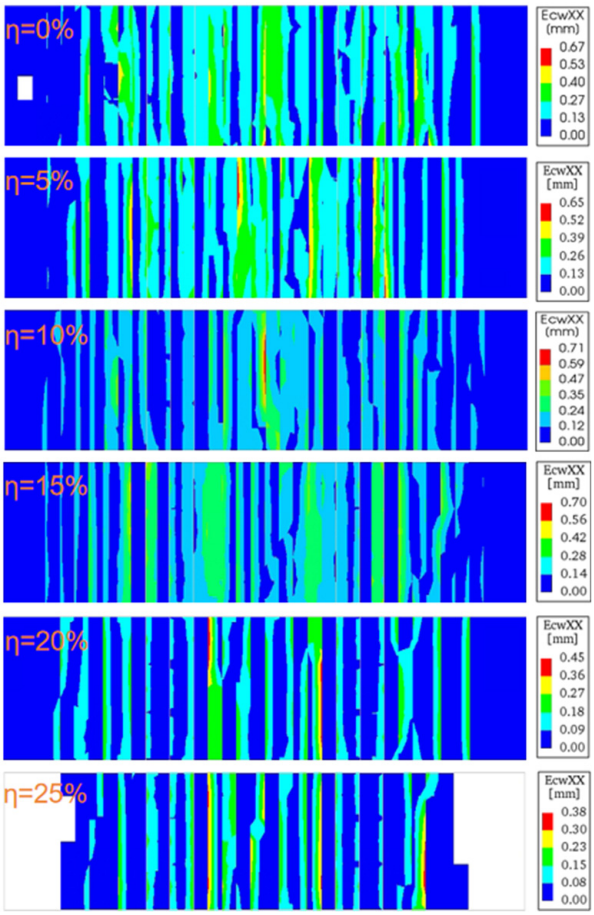
As corrosion increases to around 15%, diagonal cracks appear in the constant-moment region, marking a transition from pure flexural behaviour to flexure-shear interaction.

In the same corrosion range (approximately 5–15%), crack and strain concentration become evident near the CFRCM termination zones, where partial debonding or slip initiates. When corrosion exceeds 15%, the cracked region in both the concrete and the CFRCM shortens and the crack spacing becomes larger, leading to extensive uncracked zones away from the main flexure–shear zone. This pattern suggests that, under severe corrosion, the response is governed by a narrow, highly damaged region, while large portions of the CFRCM length are only partially mobilised.

The load capacity trends correspond closely with the observed failure patterns. At 25% corrosion, the response becomes highly localised within a narrow damaged region, which explains both the limited load recovery and the reduced utilisation of additional CFRCM layers. Around 15% corrosion, the thicker L3–L4 configurations begin to exhibit flexure–shear interaction and local slip at the CFRCM terminations, indicating the onset of over-strengthening effects. In this corrosion range, the overall strengthening trend also shifts, with a reduction in the effectiveness of the L4 scheme becoming apparent. At corrosion levels up to 15%, the predominance of uniform flexural cracking is consistent with the stable and effective strengthening performance provided by the L2 configuration.

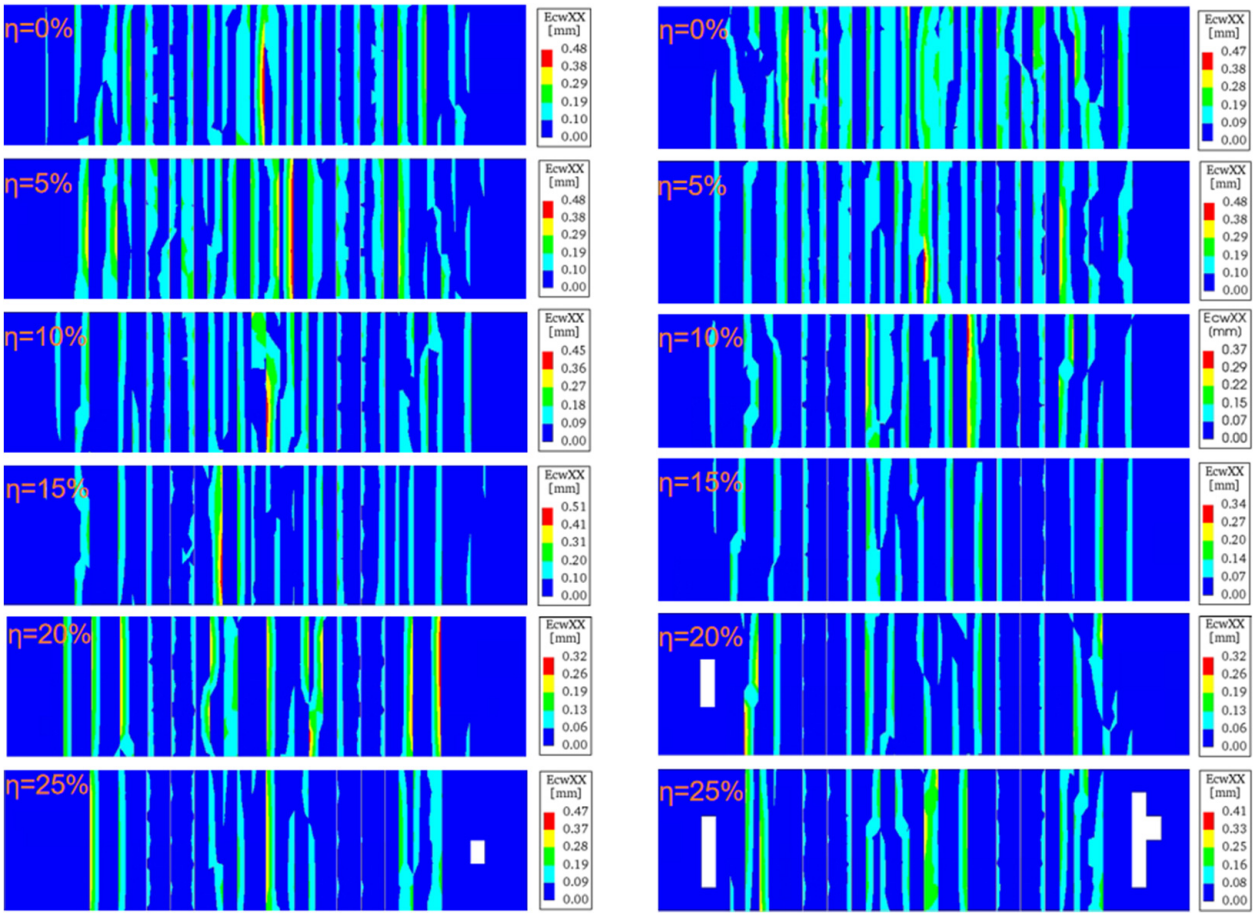


(**a**) S-B-L0-d14 series



(**b**) S-B-L1-d14 series

Figure 13. *Cont.*



(**c**) S-B-L2-d14 series (**d**) S-B-L3-d14 series

Figure 13. CFRCM crack patterns under different corrosion rates and CFRCM layer numbers.

6. Assessment of Bending Moment

6.1. Design Guidelines

Currently, ACI 549.4R-20 [53] is commonly used to evaluate the bending capacity of FRCM-strengthened members. However, given the limited contribution of the CM after cracking, the applicability of design codes originally developed for FRP systems, including ACI 440.2R-17 [17], FIB Bulletin 14 [18], and CECS 146-2003 (2007) [19], is also examined in this study. The basic assumptions include that plane sections remain plane after loading and that the bond between the FRCM and the substrate remains effective. The ultimate compressive strain limit for concrete differs across codes, with values of 0.003 in [17], 0.0035 in [18], and 0.0033 in [19]. ACI 549.4R-20 [53] characterises FRCM with bilinear tensile behaviour, considering only the second linear branch for analysis and design. In contrast, ACI 440.2R-17 [17], FIB Bulletin 14 [18], and CECS 146-2003 [19] model FRP using a linear elastic stress–strain relationship up to failure.

In terms of bending capacity calculation, all codes follow the plane section assumption and force equilibrium principles, with varying details. ACI 549.4R-20 [53] and ACI 440.2R-17 [17] address the typical balanced failure mode where steel yields before concrete crushing. FIB Bulletin 14 [18] establishes equations for two failure modes, concrete crushing following steel yielding or FRP rupture after steel yielding, with explicit definitions for the compression zone depth. CECS 146-2003 (2007) [19] covers three failure modes: balanced reinforcement, over-reinforcement with FRP reinforcement, and over-reinforcement governed by steel. Table 5 presents the formulas, with detailed calculations provided in [57].

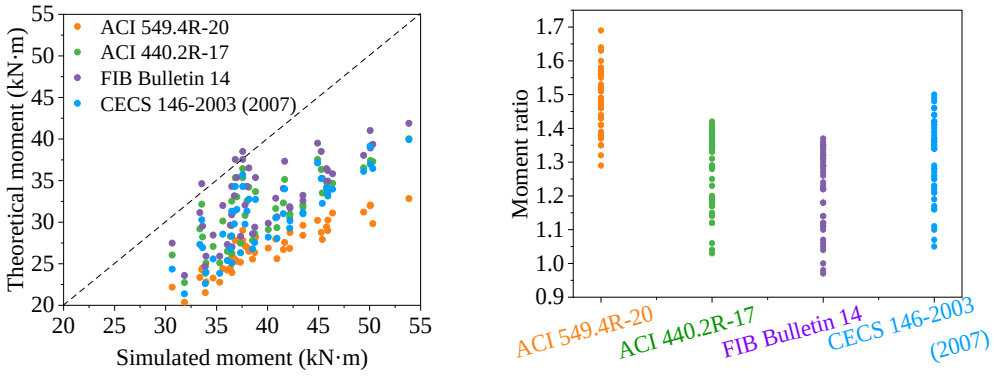
Table 5. Bending moment calculation formulas.

Design Code	Equations
ACI 549.4R-20 [53]	$M_{u1} = \Phi_m \left[A_s f_s \left(d - \frac{\beta_1 c}{2} \right) + A'_s f'_s \left(\frac{\beta_1 c}{2} - a\prime \right) + A_f f_{fe} \left(d_f - \frac{\beta_1 c}{2} \right) \right]$
ACI 440.2R-17 [17]	$M_{u2} = A_s f_s \left(d - \frac{\beta_1 c}{2} \right) + \psi_f A_f \left(d_f - \frac{\beta_1 c}{2} \right)$
FIB Bulletin 14 [18]	$M_{u3} = A_{s1} f_{yd} (d - \delta_G x) + A_f E_f \varepsilon_f (h - \delta_G x) + A_{s2} E_s \varepsilon_{s2} (\delta_G x - d_2)$
CECS 146-2003 (2007) [19]	$\xi_{cfb} h < x < \xi_b h_0$: $M_{u4} \le f_c b'_f x \left(h_0 - \frac{x}{2} \right) + f'_y A'_s (h_0 - a\prime) + \sigma_{f,md} A_f \left(h_{fe} - h_0 \right)$
	$x \le \xi_{cfb} h$: $M_{u4} \le f_c b x \left(h_0 - \frac{x}{2} \right) + f'_y A'_s (h_0 - a') + E_{cf} \varepsilon_{cf} A_{cf} (h - h_0)$
	$x < 2a$: $M_{u4} \le f_y A_s (h_0 - a') + E_{cf} \left[\varepsilon_{cf} \right] A_{cf} (h - a')$

6.2. Theoretical Bending Moment

Table 6 and Figure 14a present a comparative analysis between theoretical and simulated bending moments. It can be found that the bending moments obtained from FEA (MuFEA) are greater than those calculated using the design formulas from ACI 549.4R-20 [53] (M_{u1}), ACI 440.2R-17 [17] (M_{u2}), FIB Bulletin 14 [18] (M_{u3}), and CECS 146-2003 (2007) [19] (M_{u4}). As shown in Figure 14b, the mean values of the M_{uFEA}/M_{u1}, the M_{uFEA}/M_{u2}, the M_{uFEA}/M_{u3}, and the M_{uFEA}/M_{u4} ratios are 1.49, 1.27, 1.22, and 1.32, respectively, and the corresponding COVs are 5.80%, 8.80%, 9.80%, and 8.80%, respectively. It can be concluded that the bending capacities calculated by ACI 549.4R-20 [53] are more conservative than those obtained from ACI 440.2R-17 [17], FIB Bulletin 14 [18], and CECS 146-2003 (2007) [19]. The differences between FRP design codes are mainly due to subtle variations in calculating the compression zone height. The conservatism in ACI 549.4R-20 [53] may be attributed to its use of the elastic modulus after FRCM cracking, which is much smaller than the elastic modulus before FRCM cracking. In contrast, design guidelines for FRP systems fully account for the strength contribution of CF, as they use the elastic modulus of CF, which is significantly higher than the post-cracking elastic modulus of CFRCM.

Moreover, inspection of the subgroup results in Table 6 reveals a clear trend associated with the number of strengthening layers. As the CFRCM layer increases from L1 to L3–L4, the theoretical bending moments predicted by all design codes become progressively closer to the simulated (or experimental) values. This behaviour indicates that the additional layers in the L3–L4 configurations are not fully utilised in the actual structural response, leading to a reduced discrepancy between the code predictions. This observation is consistent with the strengthening saturation and limited layer activation identified earlier in Section 5.2.



(**a**) Simulated and theoretical moments (**b**) Moment ratios for different design codes

Figure 14. Comparisons between theoretical and simulated moments.

Table 6. Bending moment comparison.

Specimen	P_u or $P_{u,FEA}$ (kN)	Corrosion Rate (%)	M_u or $M_{u,FEA}$ (kN·m)	ACI 549.4R-13 [53]		ACI 440.2R-08 [17]		FIB Bulletin 14 [18]		CECS 146-2003 (2007) [19]	
				M_{u1} (kN·m)	M_u/M_{u1}	M_{u2} (kN·m)	M_u/M_{u2}	M_{u3} (kN·m)	M_u/M_{u3}	M_{u4} (kN·m)	M_u/M_{u4}
S-B-L1	193.72	0.00	38.74	26.35	1.47	28.62	1.35	29.40	1.32	27.55	1.41
S-B-L1-d12-η1	186.75	5.00	37.35	25.19	1.48	27.47	1.36	28.28	1.32	26.32	1.42
S-B-L1-d12-η2	182.55	10.00	36.51	23.94	1.52	26.23	1.39	27.03	1.35	25.08	1.46
S-B-L1-d12-η3	176.54	15.00	35.31	22.78	1.55	25.10	1.41	25.92	1.36	23.85	1.48
S-B-L1-d12-η4	169.44	20.00	33.89	21.53	1.57	23.86	1.42	24.68	1.37	22.61	1.50
S-B-L1-d12-η5	159.26	25.00	31.85	20.37	1.56	22.73	1.40	23.59	1.35	21.38	1.49
S-B-L2	204.02	0.00	40.80	27.96	1.46	31.64	1.29	32.88	1.24	30.52	1.34
S-B-L2-d12-η1	210.85	5.00	42.17	26.84	1.57	30.57	1.38	31.86	1.32	29.29	1.44
S-B-L2-d12-η2	204.61	10.00	40.92	25.61	1.60	29.34	1.39	30.64	1.34	28.05	1.46
S-B-L2-d12-η3	181.74	15.00	36.35	24.50	1.48	28.29	1.28	29.64	1.23	26.82	1.36
S-B-L2-d12-η4	173.32	20.00	34.66	23.28	1.49	27.08	1.28	28.44	1.22	25.58	1.35
S-B-L2-d12-η5	153.23	25.00	30.65	22.18	1.38	26.05	1.18	27.48	1.12	24.35	1.26
S-B-L3-d12-η0	229.50	0.00	45.90	29.00	1.58	34.53	1.33	36.20	1.27	33.49	1.37
S-B-L3-d12-η1	226.84	5.00	45.37	27.92	1.63	33.51	1.35	35.26	1.29	32.26	1.41
S-B-L3-d12-η2	207.70	10.00	41.54	26.70	1.56	32.31	1.29	34.06	1.22	31.02	1.34
S-B-L3-d12-η3	183.71	15.00	36.74	25.62	1.43	31.32	1.17	33.17	1.11	29.79	1.23
S-B-L3-d12-η4	178.06	20.00	35.61	24.41	1.46	30.14	1.18	32.00	1.11	28.56	1.25
S-B-L3-d12-η5	166.79	25.00	33.36	23.35	1.43	29.18	1.14	31.15	1.07	27.32	1.22
S-B-L4	251.60	0.00	50.32	29.82	1.69	37.29	1.35	39.36	1.28	36.46	1.38
S-B-L4-d12-η1	226.31	5.00	45.26	28.76	1.57	36.33	1.25	38.51	1.18	35.23	1.28
S-B-L4-d12-η2	208.37	10.00	41.67	27.55	1.51	35.14	1.19	37.33	1.12	33.99	1.23
S-B-L4-d12-η3	190.81	15.00	38.16	26.50	1.44	34.21	1.12	36.52	1.04	32.76	1.16
S-B-L4-d12-η4	184.93	20.00	36.99	25.30	1.46	33.05	1.12	35.38	1.05	31.53	1.17
S-B-L4-d12-η5	167.77	25.00	33.55	24.27	1.38	32.16	1.04	34.63	0.97	30.29	1.11
S-B-L1-d14-η0	217.37	0.00	43.47	29.62	1.47	31.83	1.37	32.58	1.33	31.01	1.40
S-B-L1-d14-η1	211.02	5.00	42.20	28.75	1.47	30.96	1.36	31.70	1.33	30.17	1.40
S-B-L1-d14-η2	200.33	10.00	40.07	26.88	1.49	29.11	1.38	29.87	1.34	28.20	1.42
S-B-L1-d14-η3	192.65	15.00	38.53	25.56	1.51	27.80	1.39	28.59	1.35	26.79	1.44
S-B-L1-d14-η4	180.27	20.00	36.05	24.23	1.49	26.50	1.36	27.31	1.32	25.38	1.42
S-B-L1-d14-η5	169.78	25.00	33.96	22.82	1.49	25.10	1.35	25.91	1.31	23.97	1.42
S-B-L2-d14-η0	231.84	0.00	46.37	31.10	1.49	34.68	1.34	35.82	1.29	33.98	1.36
S-B-L2-d14-η1	229.54	5.00	45.91	30.24	1.52	33.81	1.36	34.94	1.31	33.14	1.39
S-B-L2-d14-η2	217.29	10.00	43.46	28.42	1.53	32.04	1.36	33.23	1.31	31.17	1.39
S-B-L2-d14-η3	188.96	15.00	37.79	27.15	1.39	30.81	1.23	32.05	1.18	29.76	1.27
S-B-L2-d14-η4	182.42	20.00	36.48	25.89	1.41	29.59	1.23	30.89	1.18	28.35	1.29
S-B-L2-d14-η5	168.10	25.00	33.62	24.50	1.37	28.22	1.19	29.53	1.14	26.95	1.25
S-B-L3-d14-η0	250.40	0.00	50.08	32.07	1.56	37.41	1.34	38.92	1.29	36.95	1.36
S-B-L3-d14-η1	247.09	5.00	49.42	31.21	1.58	36.54	1.35	38.04	1.30	36.11	1.37
S-B-L3-d14-η2	228.90	10.00	45.78	29.43	1.56	34.84	1.31	36.43	1.26	34.14	1.34
S-B-L3-d14-η3	194.12	15.00	38.82	28.20	1.38	33.68	1.15	35.36	1.10	32.73	1.19
S-B-L3-d14-η4	189.89	20.00	37.98	26.96	1.41	32.53	1.17	34.30	1.11	31.32	1.21
S-B-L3-d14-η5	182.45	25.00	36.49	26.96	1.35	32.53	1.12	34.30	1.06	31.32	1.16
S-B-L4-d14-η0	269.28	0.00	53.86	32.83	1.64	40.03	1.35	41.89	1.29	39.93	1.35
S-B-L4-d14-η1	250.30	5.00	50.06	31.97	1.57	39.17	1.28	41.02	1.22	39.08	1.28
S-B-L4-d14-η2	224.51	10.00	44.90	30.22	1.49	37.54	1.20	39.51	1.14	37.11	1.21
S-B-L4-d14-η3	187.81	15.00	37.56	29.01	1.29	36.43	1.03	38.51	0.98	35.70	1.05
S-B-L4-d14-η4	184.15	20.00	36.83	27.81	1.32	35.34	1.04	37.55	0.98	34.29	1.07
S-B-L4-d14-η5	187.85	25.00	37.57	27.81	1.35	35.34	1.06	37.55	1.00	34.29	1.10
Mean	—	—	—	—	1.49	—	1.27	—	1.22	—	1.32
COV	—	—	—	—	5.90%	—	8.80%	—	9.80%	—	8.80%

7. Conclusions

In this study, we investigated the flexural performance of RC beams strengthened with the CFRCM system through finite element modelling. FEA was first conducted on the five RC beams to validate failure modes, load–displacement curves, ultimate loads, and bending capacities during loading. Subsequently, a parametric study involving 56 FEMs was carried out to evaluate the effect of CFRCM layers, rebar corrosion rate, and longitudinal reinforcement ratio. The influence of these parameters on ultimate load and failure modes was systemically examined, and the distinction in failure modes and ductility was analysed through crack patterns. Finally, the bending capacities predicted by current standards for the FRCM and FRP system were compared based on experimental and numerical results. The main conclusions are as follows:

- The CFRCM strengthening system applied in sagging-moment regions effectively improves the flexural performance of RC beams. The developed FEMs successfully reproduced the load–displacement responses, ultimate capacities, and failure modes, demonstrating its reliability for evaluating CFRCM-strengthened members. Extension of the present experimental and numerical framework to continuous RC beams, particularly in hogging-moment regions, as well as to members subjected to combined flexure–shear actions, represents a logical direction for future research.
- The number of CFRCM layers significantly influences flexural performance. A two-layer configuration provides an efficient and balanced strengthening effect, whereas additional layers yield diminishing returns due to saturation, particularly under high corrosion levels or with larger reinforcement ratios.
- The corrosion rate of steel rebar is the decisive factor for strengthening effectiveness. Full recovery of the original load capacity is only achievable when corrosion remains below a critical threshold of 15%; beyond this level, the baseline capacity cannot be restored. It should be noted that the corrosion levels considered herein represent equivalent uniform corrosion states calibrated from laboratory data.
- Corrosion rate and CFRCM layers jointly govern the failure mode. At a corrosion level of 15%, specimens strengthened with three or four CFRCM layers (L3-L4) exhibited insufficient shear resistance and developed an increased number of flexural-shear cracks.
- For practical design, a two-layer CFRCM scheme is recommended for corrosion levels up to 15%, as it offers an optimal balance between capacity recovery, crack control, and failure mode safety.
- Among the evaluated design guidelines, ACI 549.4R-20 provides the most conservative bending capacity predictions due to its reliance on the post-cracking stiffness of FRCM, whereas FRP-based codes (ACI 440.2R-17, FIB Bulletin 14, CECS 146-2003) yield less conservative and more realistic estimates.
- The study aims to extend validated experimental trends, not replace experimental work. Future work will include targeted experimental programmes focusing on high corrosion levels and CFRCM termination behaviour.

Author Contributions: Conceptualization, C.Z. and J.-P.T.; methodology, P.L. and J.-P.T.; software, R.F.; validation, C.Z., P.L. and J.-P.T.; formal analysis, P.L. and J.-P.T.; investigation, C.Z., M.Z. and L.W.; resources, R.F.; data curation, L.W.; writing—original draft preparation, C.Z. and P.L.; writing—review and editing, P.L. and J.-P.T.; visualization, C.Z.; supervision, R.F.; project administration, C.Z., L.W., M.Z. and R.F.; funding acquisition, C.Z., L.W., M.Z. and R.F. All authors have read and agreed to the published version of the manuscript.

Funding: This research was funded by National Natural Science Foundation of China (Grant Nos. 52208277/52208183/52208308/52478156/52178131), the Guangdong Basic and Applied Basic Research Foundation (Grant No. 2024A1515012190), the Shenzhen Science and Technology Program

(Grant No. JCYJ20240813105900001) and Guangdong Provincial Key Laboratory of Intelligent and Resilient Structures for Civil Engineering (2023B1212010004).

Data Availability Statement: The original contributions presented in this study are included in the article. Further inquiries can be directed to the corresponding author.

Conflicts of Interest: The authors declare no conflicts of interest.

References

1. Yi, Y.; Zhu, D.J.; Guo, S.C.; Zhang, Z.H.; Shi, C.J. A review on the deterioration and approaches to enhance the durability of concrete in the marine environment. *Cem. Concr. Compos.* **2020**, *113*, 103695. [CrossRef]
2. Lei, B.; Li, W.G.; Li, Z.H.; Wang, G.; Sun, Z.H. Effect of cyclic loading deterioration on concrete durability: Water absorption, freeze-thaw, and carbonation. *J. Mater. Civ. Eng.* **2018**, *30*, 04018039. [CrossRef]
3. Siddika, A.; Mamun, M.A.A.; Ferdous, W.; Alyousef, R. Performances, challenges and opportunities in strengthening reinforced concrete structures by using FRPs—A state-of-the-art review. *Eng. Fail. Anal.* **2020**, *111*, 104480. [CrossRef]
4. Tang, J.-P.; Feng, R.; Quach, W.-M.; Zeng, J.-J. Evaluation of flexural performance on corrosion-damaged RC beams retrofitted with UHPFRCC under marine exposure. *Eng. Struct.* **2025**, *333*, 120193. [CrossRef]
5. Qian, R.S.; Li, Q.; Fu, C.Q.; Zhang, Y.S.; Wang, Y.X.; Jin, N.G.; Jin, X.Y. Investigations on atmospheric carbonation corrosion of concrete structure beam exposed to real marine-environment for 7 years. *J. Build. Eng.* **2023**, *71*, 106517. [CrossRef]
6. Liu, D.Y.; Wang, C.; Gonzalez-Libreros, J.; Guo, T.; Cao, J.; Tu, Y.M.; Elfgren, L.; Sas, G. A review of concrete properties under the combined effect of fatigue and corrosion from a material perspective. *Constr. Build. Mater.* **2023**, *369*, 130489. [CrossRef]
7. Dogan, M. Corrosion failure in concrete reinforcement to damage during seismic. *Eng. Fail. Anal.* **2015**, *56*, 275–287. [CrossRef]
8. Tang, J.-P.; Feng, R.; Quach, W.-M.; Zeng, J.-J. Axial compressive behaviour of simulated corrosion-damaged RC columns retrofitted with UHPFRC jackets subjected to dry-wet cycling condition. *Constr. Build. Mater.* **2024**, *424*, 135956. [CrossRef]
9. Vidal, T.; Castel, A.; Francois, R. Corrosion process and structural performance of a 17 year old reinforced concrete beam stored in chloride environment. *Cem. Concr. Res.* **2007**, *37*, 1551–1561. [CrossRef]
10. Islam, M.M.; Jung, S.; Zhang, Q. Mechanical properties of corroded steel rebars after 20 years of saltwater exposure. *J. Fail. Anal. Prev.* **2022**, *22*, 1714–1724. [CrossRef]
11. Lin, H.W.; Zhao, Y.X. Effects of confinements on the bond strength between concrete and corroded steel bars. *Constr. Build. Mater.* **2016**, *118*, 127–138. [CrossRef]
12. Lin, H.W.; Zhao, Y.X.; Yang, J.Q.; Feng, P.; Ozbolt, J.; Ye, H.L. Effects of the corrosion of main bar and stirrups on the bond behavior of reinforcing steel bar. *Constr. Build. Mater.* **2019**, *225*, 13–28. [CrossRef]
13. Chong, X.; Liu, H.L.; Xie, L.L.; Zhou, A.; Huang, J.Q.; Sha, H.L. Experimental investigation of retrofitting seismically damaged reinforced-concrete frames using steel jacketing. *Structures* **2024**, *62*, 106243. [CrossRef]
14. Gao, D.Y.; Fang, D.; You, P.B.; Chen, G.; Tang, J.Y. Flexural behavior of reinforced concrete one-way slabs strengthened via external post-tensioned FRP tendons. *Eng. Struct.* **2020**, *216*, 110718. [CrossRef]
15. Siddika, A.; Mamun, M.A.A.; Alyousef, R.; Amran, Y.H.M. Strengthening of reinforced concrete beams by using fiber-reinforced polymer composites: A review. *J. Build. Eng.* **2019**, *25*, 100798. [CrossRef]
16. Wang, J.Z.; Yang, J.L.; Cheng, L. Experimental study of seismic behavior of high-strength RC columns strengthened with CFRP subjected to cyclic loading. *J. Struct. Eng.* **2019**, *145*, 04018240. [CrossRef]
17. *ACI 440.2R-17*; Guide for the Design and Construction of Externally Bonded FRP Systems for Strengthening Concrete Structures. American Concrete Institute: Farmington Hills, MI, USA, 2017.
18. *FIB Bulletin 14*; Externally Bonded FRP Reinforcement for RC Structures. International Federation for Structural Concrete: Zürich, Switzerland, 2001.
19. *CECS 146-2003 (2007)*; Technical Specification for Strengthening Concrete Structures with Carbon Fiber Reinforced Polymer Laminate. China Association for Engineering Construction Standardization: Beijing, China, 2007. (In Chinese)
20. Malumbela, G.; Moyo, P.; Alexander, M. Load-bearing capacity of corroded, patched and FRP-repaired RC beams. *Mag. Concr. Res.* **2011**, *63*, 797–812. [CrossRef]
21. Masoud, S.; Soudki, K. Evaluation of corrosion activity in FRP repaired RC beams. *Cem. Concr. Compos.* **2006**, *28*, 969–977. [CrossRef]
22. Zidani, M.H.B.; Belakhdar, K.; Tounsi, A.; Adda Bedia, E.A. Finite element analysis of initially damaged beams repaired with FRP plates. *Compos. Struct.* **2015**, *134*, 429–439. [CrossRef]
23. Jafari, A.; Shahmansouri, A.A.; Akbarzadeh Bengar, H. Hybrid CFRP–GFRP sheets for flexural strengthening of continuous RC beams: Experimentation and analytical modeling. *Struct. Concr.* **2025**, *26*, 972–993. [CrossRef]
24. Bengar, H.A.; Shahmansouri, A.A. A new anchorage system for CFRP strips in externally strengthened RC continuous beams. *J. Build. Eng.* **2020**, *30*, 101230. [CrossRef]

25. Jafari, A.; Shahmansouri, A.A.; Taslimi, A.; Naser, M.Z.; Zhou, Y. Shear capacity of FRP-RC beams: XML modeling and reliability evaluation. *Structures* **2025**, *81*, 110150. [CrossRef]
26. Jafari, A.; Shahmansouri, A.A.; Bengar, H.A.; Naser, M.Z. Post-heating flexural behavior of steel fiber reinforced SCC beams strengthened with NSM-CFRP strips: Experimentation and analytical modeling. *Constr. Build. Mater.* **2024**, *451*, 138846. [CrossRef]
27. Jabr, A.; El-Ragaby, A.; Ghrib, F. Effect of the fiber type and axial stiffness of FRCM on the flexural strengthening of RC beams. *Fibers* **2017**, *5*, 2. [CrossRef]
28. Harle, S.M. Durability and long-term performance of fiber reinforced polymer (FRP) composites: A review. *Structures* **2024**, *60*, 105881. [CrossRef]
29. Lai, B.L.; Zhou, X.; Zhang, M.Y.; Zheng, X.F.; Fan, S.G. Experimental study on the eccentric compressive behavior of steel reinforced concrete composite columns with stay-in-place ECC jacket. *J. Build. Eng.* **2025**, *102*, 112007. [CrossRef]
30. Lai, B.L.; Zheng, X.F.; Zhang, Y.X.; Zhang, M.Y.; Zhu, L.; Fan, S.G. Structural behavior of steel reinforced concrete composite columns with ECC permanent formwork: Numerical simulation and parametric study. *Structures* **2025**, *80*, 109868. [CrossRef]
31. Awani, O.; El-Maaddawy, T.; Ismail, N. Fabric-reinforced cementitious matrix: A promising strengthening technique for concrete structures. *Constr. Build. Mater.* **2017**, *132*, 94–111. [CrossRef]
32. D'Antino, T.; Carloni, C.; Sneed, L.H.; Pellegrino, C. Matrix-fiber bond behavior in PBO FRCM composites: A fracture mechanics approach. *Eng. Fract. Mech.* **2014**, *117*, 94–111. [CrossRef]
33. Liu, P.P.; Tang, J.-P.; Feng, R.; Xu, Y.; Zhu, J.-H. Experimental investigation of the shear performance of corroded RC continuous beams strengthened with polarized CFRCM plates. *Eng. Struct.* **2025**, *333*, 120145. [CrossRef]
34. Liu, P.P.; Tang, J.P.; Feng, R.; Fan, Y.H.; Zhu, J.H. Tensile behaviour and flexural performance of polarised CFRCM-strengthened corroded RC continuous beams. *Structures* **2025**, *76*, 109022.
35. Feng, R.; Tang, J.P.; Liu, P.P.; Wang, F.Y.; Zeng, J.J.; Zhu, J.H. Flexural and cracking behavior of corroded RC continuous beams strengthened with energized C-FRCM system. *Struct. Concr.* **2023**, *25*, 659–676. [CrossRef]
36. Feng, R.; Hou, L.B.; Wang, F.Y.; Thermou, G.; Xu, Y.; Zhu, J.H. Flexural performance of seawater sea sand concrete composite beams enhanced by dual-functional C-FRCM jackets. *J. Build. Eng.* **2024**, *95*, 110252. [CrossRef]
37. Elghazy, M.; El Refai, A.; Ebead, U.; Nanni, A. Effect of corrosion damage on the flexural performance of RC beams strengthened with FRCM composites. *Compos. Struct.* **2017**, *180*, 994–1006. [CrossRef]
38. Elghazy, M.; El Refai, A.; Ebead, U.; Nanni, A. Post-repair flexural performance of corrosion-damaged beams rehabilitated with fabric-reinforced cementitious matrix (FRCM). *Constr. Build. Mater.* **2018**, *166*, 732–744. [CrossRef]
39. Elghazy, M.; El Refai, A.; Ebead, U.; Nanni, A. Corrosion-damaged RC beams repaired with fabric-reinforced cementitious matrix. *J. Compos. Constr.* **2018**, *22*, 04018039. [CrossRef]
40. Escrig, C.; Gil, L.; Bernat-Maso, E. Experimental comparison of reinforced concrete beams strengthened against bending with different types of cementitious-matrix composite materials. *Constr. Build. Mater.* **2017**, *137*, 317–329. [CrossRef]
41. Ebead, U.; El-Sherif, H. Near surface embedded-FRCM for flexural strengthening of reinforced concrete beams. *Constr. Build. Mater.* **2019**, *204*, 166–176. [CrossRef]
42. Sneed, L.H.; Verre, S.; Carloni, C.; Ombres, L. Flexural behavior of RC beams strengthened with steel-FRCM composite. *Eng. Struct.* **2016**, *127*, 686–699. [CrossRef]
43. Bencardino, F.; Carloni, C.; Condello, A.; Focacci, F.; Napoli, A.; Realfonzo, R. Flexural behaviour of RC members strengthened with FRCM: State-of-the-art and predictive formulas. *Compos. Part B Eng.* **2018**, *148*, 132–148. [CrossRef]
44. Zhu, X.M.; Su, M.N.; Wang, Y. Improved methods to predict the effective strain for the design of RC beams strengthened by FRCM composite. *Structures* **2024**, *61*, 106079. [CrossRef]
45. Jung, K.; Hong, K.; Han, S.; Park, J.; Kim, J. Prediction of flexural capacity of RC beams strengthened in flexure with FRP fabric and cementitious matrix. *Int. J. Polym. Sci.* **2015**, *1*, 868541. [CrossRef]
46. Zhou, F.; Xu, W.; Du, Y.; Peng, H. Flexural strengthening of reinforced concrete beams with prestressed and unprestressed fabric-reinforced cementitious plates. *Adv. Struct. Eng.* **2018**, *21*, 975–989. [CrossRef]
47. Wei, L.L.; Ueda, T.; Matsumoto, K.; Zhu, J.H. Experimental and analytical study on the behavior of RC beams with externally bonded carbon-FRCM composites. *Compos. Struct.* **2021**, *273*, 114291. [CrossRef]
48. Mandor, A.; El Refai, A. Flexural response of reinforced concrete continuous beams strengthened with fiber-reinforced cementitious matrix (FRCM). *Eng. Struct.* **2022**, *251*, 113557. [CrossRef]
49. Mandor, A.; El Refai, A. Theoretical investigation of the structural performance of multi-span reinforced concrete beams strengthened with FRCM systems. *Eng. Struct.* **2024**, *308*, 117994. [CrossRef]
50. Elghazy, M.; El Refai, A.; Ebead, U.; Nanni, A. Experimental results and modelling of corrosion-damaged concrete beams strengthened with externally-bonded composites. *Eng. Struct.* **2018**, *172*, 172–186. [CrossRef]
51. Aljazaeri, Z.R.; Al-Jaberi, Z. Numerical study on flexural behavior of concrete beams strengthened with fiber reinforced cementitious matrix considering different concrete compressive strength and steel reinforcement ratio. *Int. J. Eng.* **2021**, *34*, 793–802. [CrossRef]

52. Taie, B.; Mandor, A.; El Refai, A. Experimental and numerical investigation of two-span RC beams strengthened with fiber-reinforced cementitious matrix (FRCM). *Eng. Struct.* **2024**, *300*, 117246. [CrossRef]
53. *ACI 549.4R-20*; Guide to Design and Construction of Externally Bonded Fabric-Reinforced Cementitious Matrix (FRCM) Systems for Repair and Strengthening Concrete and Masonry Structures. American Concrete Institute: Farmington Hills, MI, USA, 2020.
54. Manie, J.; Kikstra, W.P. *DIANA Finite Element Analysis, Release 9.4.4 User's Manual*; TNO DIANA BV: Delft, The Netherlands, 2014.
55. Hordijk, D.A. Local Approach to Fatigue of Concrete. Ph.D. Thesis, Delft University of Technology, Delft, The Netherlands, 1991.
56. Feenstra, P.H. Computational Aspects of Biaxial Stress in Plain and Reinforced Concrete. Ph.D. Thesis, Delft University of Technology, Delft, The Netherlands, 1993.
57. Feng, R.; Liu, P.P.; Zhang, J.Z.; Wang, F.Y.; Xu, Y.; Zhu, J.H. Bending behaviour of corroded RC continuous beams with C-FRCM strengthening system. *J. Build. Eng.* **2022**, *60*, 105229. [CrossRef]
58. *GB 50010-15*; Code for Design of Concrete Structures. Ministry of Housing and Urban-Rural Development of the People's Republic of China: Beijing, China, 2015. (In Chinese)
59. *ACI 318-08*; Building Code Requirement for Structural Concrete and Commentary. American Concrete Institute: Farmington Hills, MI, USA, 2008.
60. *FIB Bulletin 65*; FIB Model Code for Concrete Structures 2010. International Federation for Structural Concrete: Lausanne, Switzerland, 2012.
61. Li, X.Q.; Zhang, T.; Ding, Z.D.; Yang, X.; Wen, J.C. Numerical analysis of normal concrete lining strengthening methods under different damage levels. *Struct. Infrastruct. Eng.* **2021**, *17*, 1597–1611. [CrossRef]
62. Liu, P.P.; Tang, J.P.; Feng, R.; Fan, Y.H.; Zhu, J.H. Interfacial behaviour and shear performance of polarized CFRCM-strengthened corroded RC continuous beams. *Constr. Build. Mater.* **2025**, *472*, 140786. [CrossRef]
63. Li, Y.H.; Zheng, S.S.; Dong, L.G.; Wen, G.F. Tensile properties test and simulation of non-uniform corroded reinforcement. *J. Build. Mater.* **2022**, *25*, 991–998.
64. CEB-FIP Model Code. In *Design of Concrete Structures*; British Standard Institution: London, UK, 1993.
65. Liu, J.R.; Zhang, D.W.; Xie, Z.Y.; Zhu, J.H.; Lai, Y.B. Effect of anchorages on C-FRCM/concrete interfacial shear performance. *Constr. Build. Mater.* **2024**, *431*, 136518. [CrossRef]
66. Zargarian, M.; Rahai, A. An experimental and numerical study on continuous RC deep beams strengthened with CFRP strips. *Int. J. Civ. Eng.* **2022**, *20*, 619–637. [CrossRef]

Disclaimer/Publisher's Note: The statements, opinions and data contained in all publications are solely those of the individual author(s) and contributor(s) and not of MDPI and/or the editor(s). MDPI and/or the editor(s) disclaim responsibility for any injury to people or property resulting from any ideas, methods, instructions or products referred to in the content.